Fall 2020

Design, Discovery, and Characterization of Single Crystals of a Topological Semimetal Using a Self-Flux Method

Sudha Krishnan
Missouri State University, Sudha1916@live.missouristate.edu

DESIGN, DISCOVERY, AND CHARACTERIZATION OF SINGLE CRYSTALS OF A TOPOLOGICAL SEMIMETAL USING A SELF-FLUX METHOD

A Master's Thesis

Presented to

The Graduate College of

Missouri State University

In Partial Fulfillment

Of the Requirements for the Degree

Master of Science, Materials Science

By

Sudha Krishnan

December 2020

DESIGN, DISCOVERY, AND CHARACTERIZATION OF SINGLE CRYSTALS OF A TOPOLOGICAL SEMIMETAL USING A SELF-FLUX METHOD

Physics, Astronomy, and Materials Science

Missouri State University, December 2020

Master of Science

Sudha Krishnan

ABSTRACT

Realization of topological semimetals in the recent past show that ternary intermetallics can exhibit topological phases. This discovery initiated the quest for this novel research. There is a crucial need to discover new materials that manifest these phases for a better understanding of their behavior to utilize them in device technology. Also, Bi compounds have attracted much attention as candidates for topological materials and topological superconductors. In this context, synthesis and characterization of single crystals of a layered transition metal pnictide $SmMnBi_2$, a potential Dirac topological semimetal candidate, is reported. A flux method was utilized to synthesize single crystals of $SmMnBi_2$ and crystallographic data revealed properties isostructural to the recently reported topological semimetal compounds $EuMnBi_2$ and $YbMnBi_2$. The motivation behind this research work is to employ flux method to discover new materials with exotic behaviors in order to expand the field of topological semimetals.

KEYWORDS: topological phases, Weyl, Dirac, semimetals, crystal growth, flux

DESIGN, DISCOVERY, AND CHARACTERIZATION OF SINGLE CRYSTALS OF A TOPOLOGICAL SEMIMETAL USING A SELF-FLUX METHOD

By

Sudha Krishnan

A Master's Thesis
Submitted to the Graduate College
Of Missouri State University
In Partial Fulfillment of the Requirements
For the Degree of Master of Science, Materials Science

December 2020

Approved:

Tiglet Besara, Ph.D., Thesis Committee Chair
Ridwan Sakidja, Ph.D., Committee Member
Kartik C. Ghosh, Ph.D., Committee Member
Julie Masterson, Ph.D., Dean of the Graduate College

ACKNOWLEDGEMENTS

I would like to express my appreciation and thanks to my advisor Dr. Tiglet Besara for his immense support and guidance throughout this experience. I would also thank Dr. Kartik C Ghosh and Dr. Sakidja Ridwan for serving as my committee members. I offer my sincere appreciation for the learning opportunities provided by all the faculties, and staff in Physics, Astronomy, and Materials Science Department.

A special thanks to my family Mr. Natarajan, Akshara, and Akhil.

I extend my thanks to my family friend Mr. Sultan Zahirsha as well.

TABLE OF CONTENTS

LIST OF TABLES

LIST OF FIGURES

INTERMETALLICS AND TOPOLOGICAL SEMIMETALS

Introduction

The discovery of topological semimetals have established a new impetus to the research which includes the prediction of new semimetal phases, the realization of new materials types, and the exploration of their properties as well as potential for application into devices [1]. Material with intriguing physical properties can be achieved through different combination of chemical constituents and one of such types is ternary intermetallics. The motivation for this research is the exploratory growth of ternary intermetallics using flux method and investigation of their fundamental properties. An outline of key characteristics of such intermetallic compounds is that (i) it can be formed by at least two metals, and (ii) atomic bonding becomes directional, meaning the bonded atom prefer specific orientation relative to one another, and this in turn gives molecules a definite shape [2].

There are several techniques with unique capabilities available in the synthetic toolbox of solid-state research and they generally involve high temperatures. The reason being the starting materials of these reactions are usually solids themselves and therefore high temperatures are required to allow sufficient diffusion to initiate the reaction. One of the synthetic roadblocks of high temperature growths is thermodynamically stable binaries: the growth generally yields stable binaries which is difficult to circumvent due to their structural stability [3].

Topological Semimetals

The study of electronic structure topology of crystalline materials have sparked interest in the past decade as the new frontier in the field of quantum materials. The field of topology in

condensed matter physics originated from the concept that the electronic band structure of certain type of insulators are significantly different from the trivial insulators. The timeline of development in the field of topological semimetal is shown in Figure 1.1.

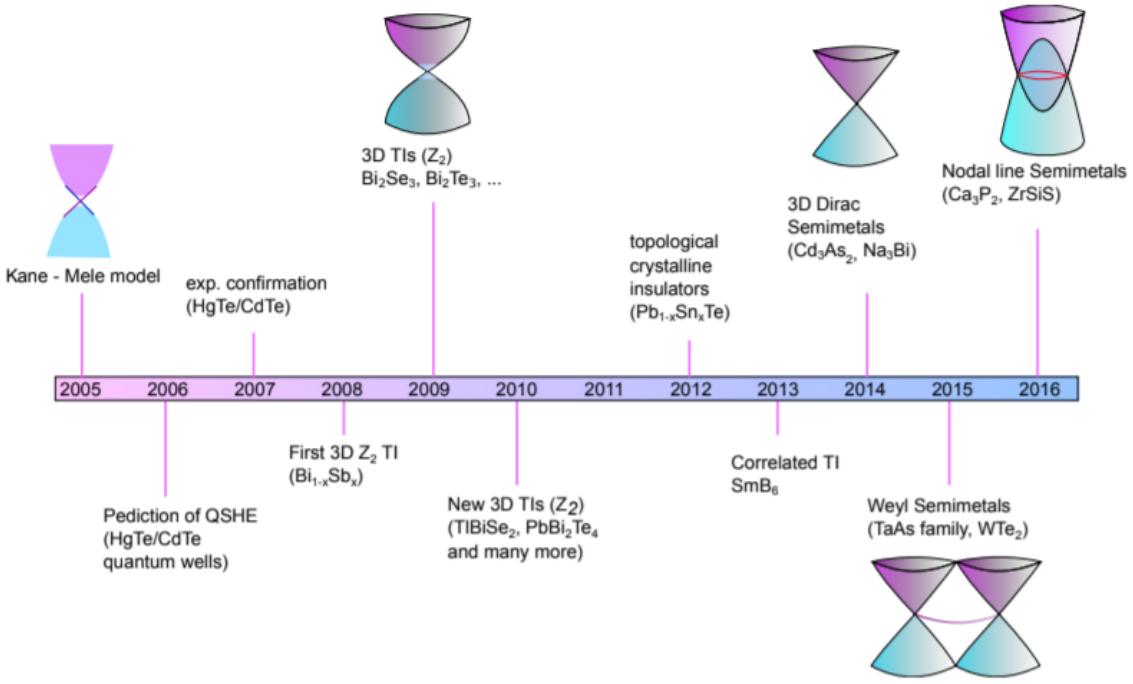

Figure 1.1. Timeline of development in the field of topological semimetals [4].

The underlying hypothesis is when two insulators of different topologies are brought together, an interface with zero mass electrons that resists backscattering would appear between them [4]. The discovery of topological insulators initiated the search for a new type of topological materials, and the attention has turned towards topological semimetals and metals in the recent past [5]. Topological semimetals are quantum phases of matter that hosts Dirac or Weyl fermions. The idea that metals can have a topologically nontrivial electronic structure is not completely new, although it was first theorized as Weyl fermions by the mathematician and

physicist Herman Weyl in 1929 [6]. Later, Weyl fermions were experimentally observed in the synthetic crystals of tantalum arsenide (TaAs) in 2015. These Weyl fermions do not bear any mass and they travel unusually fast on the surface of the crystal with no backscattering, which hinders efficiency and generate heat in normal electronic material. The Weyl fermions can be observed either in noncentrosymmetric or magnetic material with spin-orbit coupling. With this in focus, the experimental realization of both Weyl and Dirac semimetals within the recent couple of years has brought the field to the forefront of quantum condensed matter research.

The band theory of solids classified the common materials as insulators, semimetals, or metals. A finite energy gap separates the conduction and valence bands in an insulator according to their electronic structures. Over the last decade, insulators can be further classified into different classes based on the topology of the band structures. For example, the ordering of the valence and conduction band of an ordinary insulator can be inverted by strong spin-orbit coupling and can be transformed into topological insulators (see Figure 1.2).

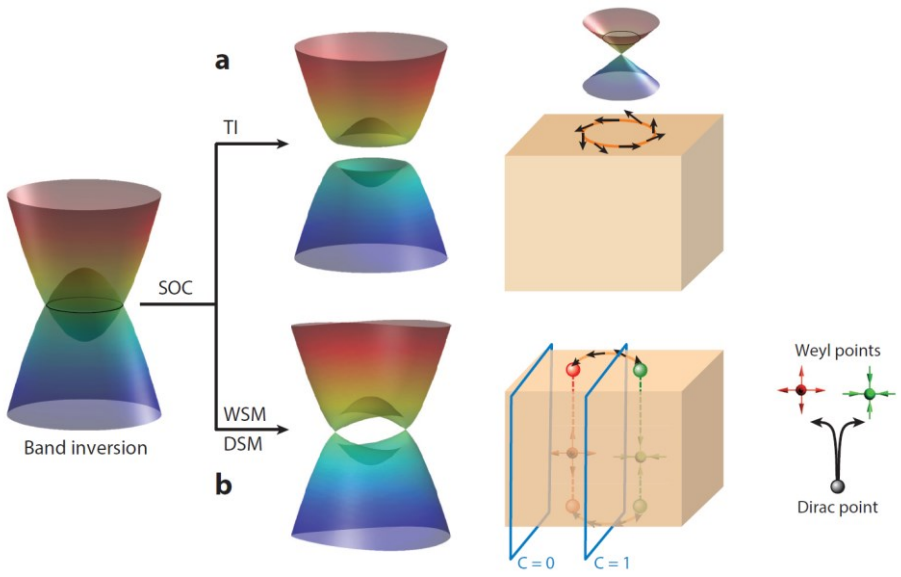

Figure 1.2. Classification based on spin-orbit coupling (a) topological insulator (b) Weyl semimetal or Dirac semimetal [7].

This inverted bulk band structure give rise to metallic surface states, which demonstrate a Dirac cone-like dispersion known as Dirac semimetals. These topological surface states are also observed in many exotic semimetals known as Weyl semimetals. The Weyl semimetals are characterized by the existence of topological Fermi arcs on the surface and chiral magnetic effects in the bulk [7].

Figure 1.3 shows typical schematic diagrams of the band structures of topological and trivial semiconductors. Weyl semimetals can occur in crystals either with a broken spatial-inversion symmetry (IS), broken time-reversal symmetry (TRS), or both. Examples of the first type (with only broken lattice inversion symmetry) were observed in 2015, but realizations of Weyl semimetals with broken time reversal symmetry are still rare. Recently, the layered intermetallic compound $YbMnBi_2$ has been proposed as a potential candidate of a magnetic Weyl semimetal [9].

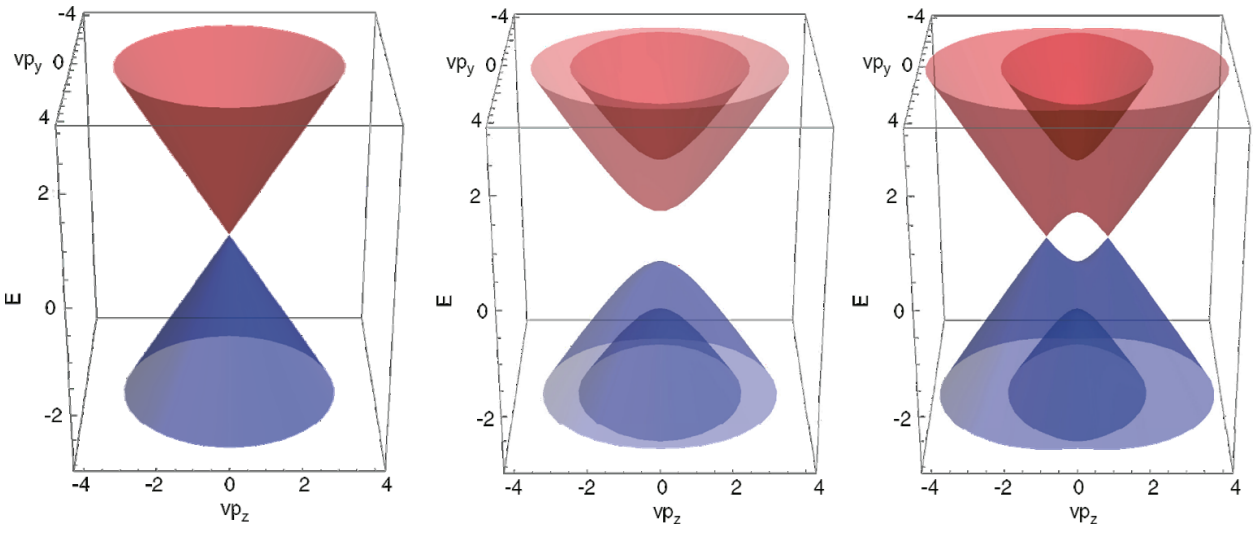

Figure 1.3. Band diagram of topological semimetals, (left) Dirac semimetal, (middle) trivial semiconductor, (right) Weyl semimetal [8].

The focus of this work is to explore such novel quantum materials exhibiting exotic properties. The impetus here is exploration, synthesis, and characterization of topological semimetals such as layered manganese pnictides having a general structural formula (*AE,Ln*)$MnBi_2$ (*AE* = alkaline earth metals, *Ln*=lanthanides).

Potential Applications

The topological semimetals bridges the world of topology and magnetism exhibiting exotic behavior which not only have fundamental scientific importance but may promise great potential for various applications is shown in Figure 1.4. New material under this category provide exciting possibilities for integration into technology.

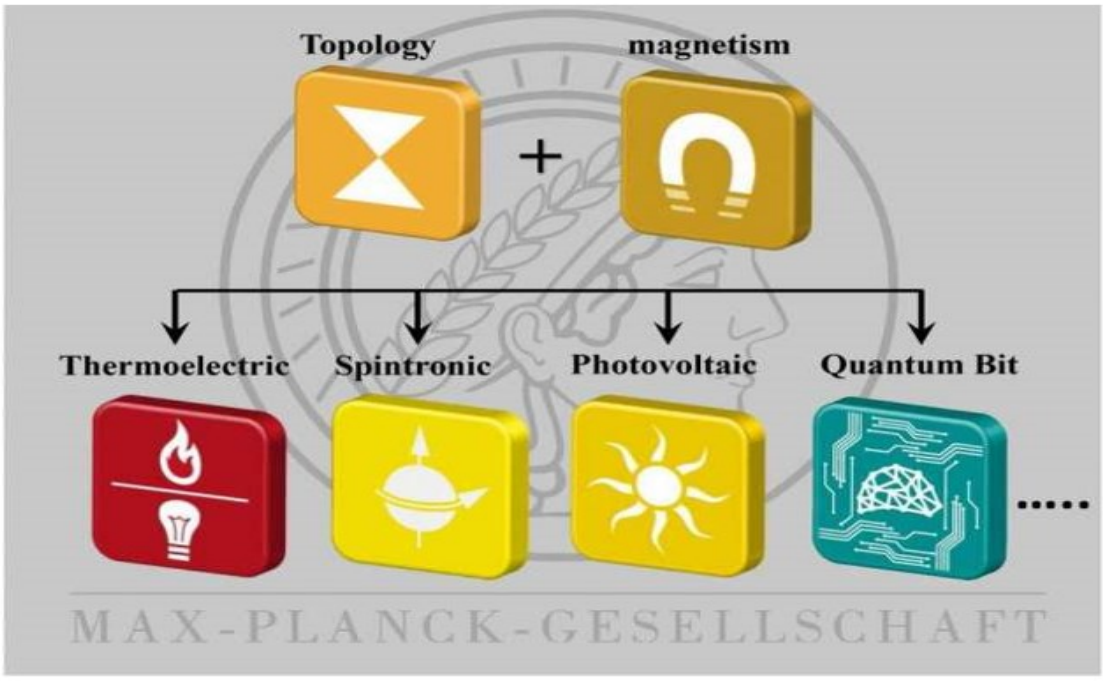

Figure 1.4. Potential applications of Weyl semimetals [10].

Topological semimetals exhibit exceptional electronic transport properties (e.g. extremely high carrier mobility and large linear magnetoresistance) and tuning these properties could help develop a new generation of spintronic devices with low power consumption [11]. The quality of sensing and detecting devices depends on the intrinsic optical properties of the material. Devices like infrared photodetectors utilizes short intrinsic response times to operate at high frequencies. Rapid photorelaxation has been seen in all kinds of Dirac semimetals that could be incorporated in optical devices. Topological materials are sensitive to defects or other kinds of disorder, which provide a perfect platform to understand surface states such as heterogenous catalysis. Topological semimetal with the combination of electronic structure and low thermal conductivity could provide a platform for energy conversion applications [12].

GROWTH OF SINGLE CRYSTALS

Overview and History

The antiqueness of the crystal can be traced back to prehistoric ages where humans had been enticed by crystals like gemstones as beautiful ornaments, religious symbols, and lucky charms. Although man practiced crystal growth and crystallization as early as 1500 BC, in the form of salt and sugar crystallization, single crystals are now fundamental pillars of our emerging, modern technology. Crystal growth is a relatively new industry and has been one of the fascinating fields of research owing to the crystals' large-scale applications for devices. Probing of single crystals are often necessary to understand the intrinsic properties of the material. The systematic approach to crystal growth began during the latter half of the 19th century, and it relied on the concept of Gibb's phase equilibria from a thermodynamical point of view. The phase equilibria studies play an important role in interpreting crystallizing phases and their crystallization boundaries of a given system for the successful growth of single crystals [13].

Symmetry, molecular structure, purity, and physiochemical environment of the formations are the major factors that influence the growth and shape of crystals, as well as provide unique physical and chemical properties. These properties would eventually bring in a dramatic change in the modern device industry [14]. In present day, artificially grown crystals find applications in a variety of fields, such as electronics, electro-optics, spintronics, magnetic devices, optics, oscillators, polarizers, transducers, radiation detectors, lasers, etc. [14]. Synthesis of single crystals might be a challenging process, and the extra effort is worth if they

have exceptional benefits [15]. Single crystals have a high degree of order structure in contrast to polycrystalline material which has several disadvantages.

Theories of Crystal Growth

The most fundamental attribute of phase transformation is the formation of a new phase in the body of a parent phase such as solid, liquid, vapor, or ions. When the crystal is in dynamic equilibrium with the parent phase, the available free energy is minimum and consequently hinders the growth process [14]. This means any decrease in the free energy associated with the crystallization process impedes the growth of crystals. Hence, the system has to overcome this potential barrier by changing pH, pressure, chemical potential, temperature, electrochemical potential, strain, etc. This would add up free energy to facilitate growth. This beginning phase of first order transition is termed nucleation. The nucleus may either emerge in the homogenous bulk or heterogeneously on an alien surface or on an impurity. For the crystal growth to be initiated, a driving force is required which is retrieved either by supersaturating a solvent or by supercooling a liquid or gas phase. A steady-state supersaturation or supercooling will aid in the growth of high-quality crystals and therefore centers of nucleation or crystallization centers play a key role towards crystal growth. Gibbs was the first to formulate that the development of small embryonic clusters are needed for the growth of macroscopic crystals. Gibbs-Thomson equation for the nucleation from solution is [14]

$$k_B T \ln\left(\frac{C}{C^*}\right) = \frac{2\sigma V}{r}, \quad (2.1)$$

where C is the actual concentration, C* is the concentration of the solution with a crystal of infinite radius r, k_B is the Boltzmann constant, σ is the surface energy per unit area, V is the volume of the growth units, and T is the temperature of the crystal.

Crystal Growth Techniques. Crystal growth is a chemical process that incorporates solid, liquid, or gas either separately or together to form a homogenous solid substance having three-dimensional atomic arrangement. Single crystal growth is ascribed to the phase transformation into the solid-state form from one of the three general classifications:

1. Solid – Solid phase transformation.
2. Liquid – Solid phase transformation.
3. Vapor – Solid phase transformation.

The solid to solid technique is rarely used, while, on the other hand, there are a variety of different techniques available for the liquid to solid phase transformation and vapor to solid phase transformation techniques (see Figure 2.1) [14]. These two techniques are widely used in crystal growth.

Solid Growth. Atomic diffusion is the controlling element of this technique and is a reliable one for ionic conductors or superionic conductors where the small cation is quite mobile at normal temperatures. Solid growth techniques are of least significance, yet the methods such as sintering, annealing, quenching, heat treatment are widely used in metallurgical processes in tuning the material properties [16].

Vapor-Phase Growth. The vapor phase growth technique is the simplest method available to produce high purity crystals and is suitable for industries which require mass production of crystals for electronic devices due to their low cost and high throughput [14]. This process is carried out in three phases: vaporization, then transport, followed by deposition. Initially, this technique was utilized to grow high quality bulk crystals like CdS and HgI_2 [16] and now widely used to grow thin films, epitaxial layers, and substrates in the field of semiconductor technology.

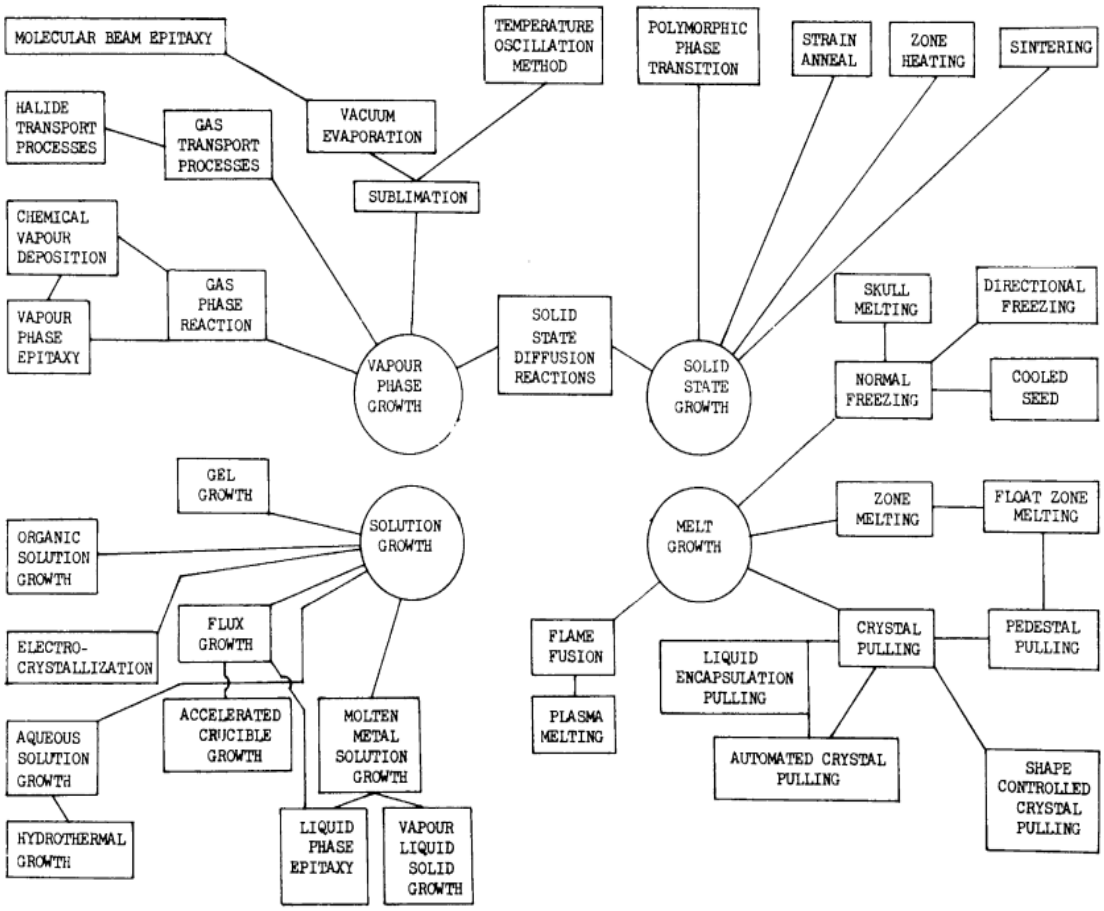

Figure 2.1. Crystal growth techniques [16].

Solution Growth. Often, melt growth merges into solution growth and the major differences between these two growth methods are that in melt growth, the solvent freezes well below its melting point, while in solution growth, the solute crystallizes well below its melting point [16]. Solution growth method is widely used for growing technologically important crystals as well as for a various other crystalline product for daily life such as growth of medicines, foods, fertilizers, and pesticides [14,16]. They are suitable for substances which melt incongruently, and for substances that decompose below the melting point. Solution growth has

an excellent control over the growth temperature and viscosity. The simplicity of the equipment, control over the growth temperature, and high degree of crystal perfection due to their growth taking place well below the melting point are the advantages of the solution growth technique [14]. Here again, there are three major classifications in solution growth based on the pressure, the temperature, and the nature of the solvent and the solute:

1. Low temperature aqueous solution growth.
2. Superheated aqueous solution growth.
3. High temperature solution growth.

High Temperature Solution Growth. The solution growth widely recognized as flux growth is a technique of growing wide range of complex materials from molten salt solvent. In this method, the starting materials of the desired compound are dissolved in a solvent called flux in a fixed proportion. The solute-solvent ratio determines the growth temperature of this method. In this process, the growth of the desired compound takes place well below the melting point of the solute material, which is the benefit of using this technique. Due to the reduced growth temperature, the product of this approach yields high quality single crystals free from point defects, dislocation, or grain boundaries in contrast to materials grown from other techniques. The relatively low growth temperatures and slow cooling rates utilized in the flux method can diminish the thermal strains of the grown crystals. This method has a few drawbacks as well, such as small crystal sizes due to multinucleation and frequently developing facets making it difficult to determine the linear growth rate which can develop surface inhomogeneities, which may be a downside for the industrial production. Another limitation to this approach is incorporation of impurities in the form of ions of the flux material [14]. Nonetheless, despite

these disadvantages, the flux technique is widely used for reasons that it needs relatively little effort to grow crystals compared to other methods and it requires no specialized equipment. The crystal formation occurs with the following three steps:

1. Achievement of supersaturation or supercooling.
2. Nucleation.
3. Growth of the nuclei into the single crystal of different phase.

Achievement of Supersaturation or Supercooling. The crystallization process takes place in multiple stages. The initial stage is the formation of supersaturated solution because the phase transition can happen only when a system is in a nonequilibrium condition. During the second stage, supercooling occurs where the molecules dissolved in solution begin to agglomerate to relieve the supersaturation and attains equilibrium. The formation of nuclei takes place at this stage and they can act as the centers of crystallization [17]. Supersaturation and supercooling are two of the most common driving forces behind the crystal formation. The driving forces for the nucleation of new phase is the difference between the chemical potentials μ_m and μ_c of the growth unit in the mother and crystalline phase:

$$\Delta\mu = \mu_m - \mu_c \qquad (2.2)$$

When $\Delta\mu > 0$, the system is said to be supersaturated. This is the thermodynamic condition essential for the nucleation and growth phase. On the other hand, if $\Delta\mu < 0$, the system is said to be undersaturated and under such conditions, crystals will dissolve. When $\Delta\mu = 0$, the mother phase is in equilibrium with the crystalline phase [18]. From this it is inferred that at a given temperature *T*, pressure *P*, and concentration,

$$\mu^e = \mu_m \qquad (2.3)$$

Where μ^e is the chemical potential of the solute molecule in equilibrium phase between the crystalline and mother phases. Hence,

$$\Delta\mu = \mu_m - \mu^e \qquad (2.4)$$

For the crystallization from solution, the level of supersaturation is

$$\sigma = \frac{C - C_e}{C_e} \qquad (2.5)$$

where C_e is the threshold concentration of standard solution and C is the actual solute concentration.

The difference in chemical potentials between the solution phase and crystal phase can be expressed as follows,

$$\Delta\mu = kBT \ln\frac{C}{C_e} = kBT \ln (1 + \sigma) \quad (2.6)$$

If $\sigma < 1$, after approximation using Taylor series expansion as

$$\frac{\Delta\mu}{k_B T} \approx \sigma \quad (2.7)$$

Thermodynamics and Kinetics

According to theory, the process of crystallization begins when the concentration of a compound in a solvent exceeds the solubility limit whereas practically this process is impeded kinetically, and therefore crystals begin to grow only from supersaturated solutions. It is clear that the supersaturation is the driving force in the crystallization process, and therefore knowledge about what amount of solute can be dissolved in the solvent and what amount of solute will remain in the mother liquid at the end is essential. Saturation is an equilibrium condition. This state of equilibrium can be disturbed to show appreciable degrees of

supersaturation by slowly cooling the saturated solution without disturbance. This is vital for a successful crystallization process.

Figure 2.2 helps in understanding the thermodynamic relationship of the crystal growth. It illustrates three zones: (i) the stable zone where crystallization is not possible, (ii) the metastable zone where spontaneous crystallization is improbable, and (iii) the unstable zone where spontaneous crystallization is probable, but not certain.

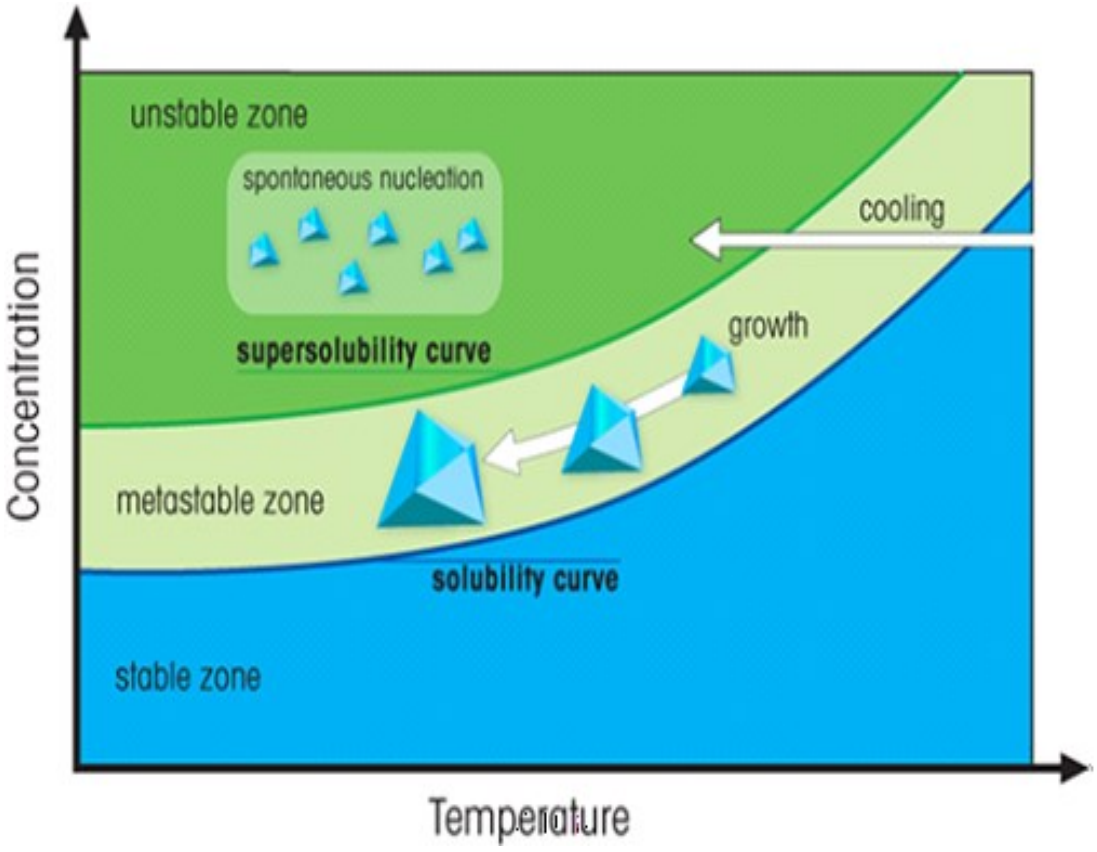

Figure 2.2. Thermodynamics of crystal growth [19].

The level of supersaturation decides the efficiency of the process of crystallization. Crystallization is preceded by nucleation, which happens either spontaneously or is induced by vibration, stress or foreign particles. On rapid cooling, nucleation sets in too quickly resulting in

the growth of too many small crystals, whereas crystals of large sizes are the desired product of the crystallization process. Large crystals can be synthesized by preventing too many nucleation sites. Crystals that grow more slowly tend to be larger, and this can be achieved by reducing the concentration slowly down to the metastable zone where a small number of larger crystals are probable. This process can be accomplished by utilizing methods such as evaporation or slow cooling.

Evaporation. In this method, the concentration of the solvent increases until supersaturation is reached because of gradual loss of solvent due to evaporation. This is followed by nucleation and then crystallization as illustrated in Figure 2.3. The evaporation rate depends on the number and size of the holes on the cover of the container. This method is not suitable for highly volatile solvents and materials that are sensitive to air.

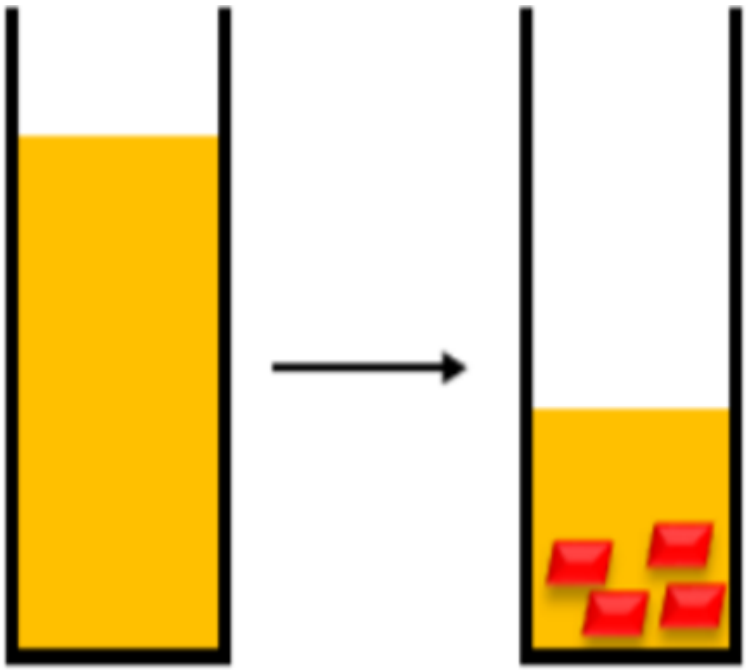

Figure 2.3. Illustration of evaporation method.

Slow Cooling. Slow cooling method is the easiest method to grow bulk single crystals from the solution. As illustrated in Figure 2.4, the solution becomes saturated during the cooling process resulting in nucleation sites which grow overtime to form crystals. This method is not good for small amounts of material.

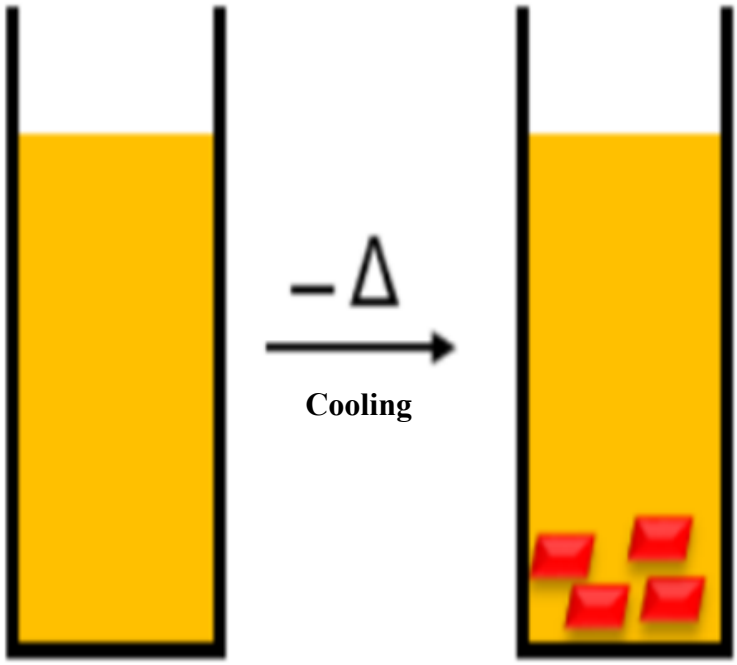

Figure 2.4. Illustration of slow cooling method.

Nucleation

Crystallization from solutions can be divided into multiple stages. The initial stage is the formation of supersaturated solution. In the next stage, the dissolved molecules in the solution start to agglomerate and the system tend to move towards equilibrium. This process of molecular agglomeration leads to the formation of nuclei that can act as centers of crystallization. Thus, nucleation is defined as the process of formation of nanoscopically tiny clusters of the new crystalline phase that can grow spontaneously to macroscopic sizes.

Nucleation that take place spontaneously from a previously crystal free solution is referred as primary nucleation and that arise in the presence of the preexisting parent crystal of the same solute in the solution is referred as secondary nucleation. Primary nucleation can be either homogenous or heterogenous based on the influence of foreign bodies. [17]

Gibbs was the first to define the change in free energy required in the formation of cluster (ΔG) as the sum of change in free energy for the phase transformation (ΔG_{ph}) and the change in free energy for the surface formation (ΔG_s)

$$\Delta G = \Delta G_{ph} + \Delta G_s = \beta L^2 \sigma + \alpha L^3 \Delta G_{ph} \qquad (2.8)$$

Where σ is the surface tension, α is the volume shape factor, β is the area shape factor, and L is the characteristic length. For a sphere of clusters with radius r, the change in Gibb's free energy becomes,

$$\Delta G = 4\pi r^2 \sigma + \frac{4}{3} \pi r^3 \sigma \Delta G_{ph} \qquad (2.9)$$

For crystallization from solutions, the second term (ΔG_{ph}) relates the spontaneous tendency of a supersaturated solution to undergo deposition. Because the solid state is more stable than the liquid (i.e., $\mu_{solid} < \mu_{liquid}$), ΔG_{ph} becomes negative, therefore the change in Gibbs free energy of the system decreases which promotes growth. On the other hand, introduction of a solid–liquid interface increases the free energy by an amount proportional to the surface area of the cluster. As a result, the change in surface free energy ΔG_s increases, which facilitates dissolution [17].

Figure 2.5 illustrates the free energy change against cluster formation. The change in surface free energy ΔG_s term is positive and dominates at small radii due to which an increase in total free energy change is observed. This leads to the smallest clusters in a solution to dissolve. As cluster size increases, the competition between the positive ΔG_s and negative ΔG_{ph} terms

becomes significant, and total free energy goes through a maximum at a value of r called the critical size r_c. Therefore, the growth becomes energetically favorable for cluster sizes above the critical radius r_c,

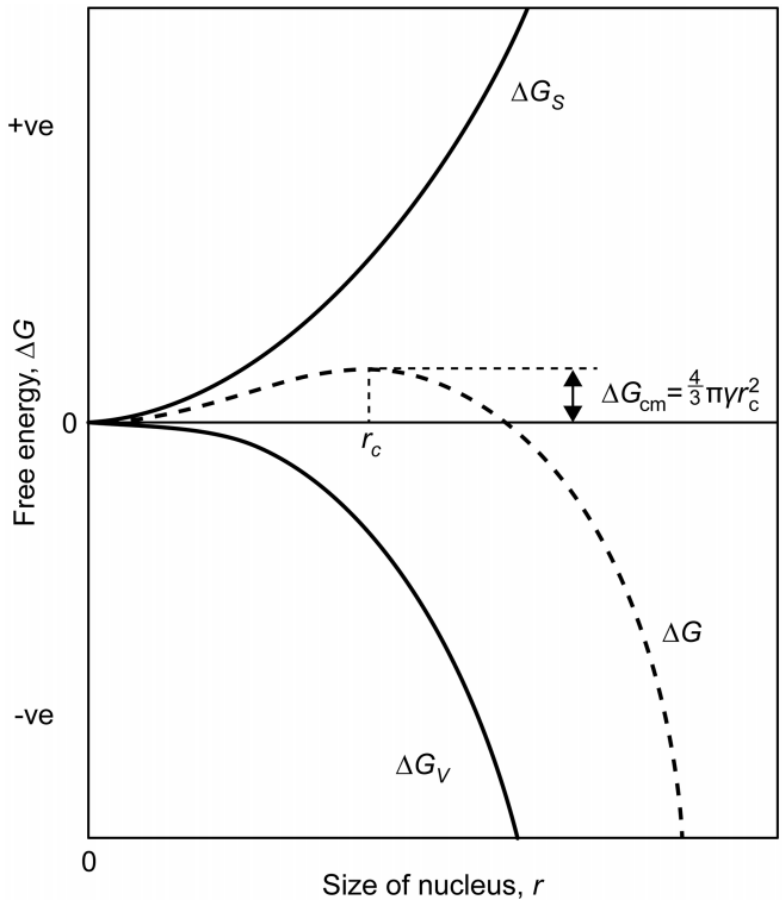

Figure 2.5. Free energy versus cluster size [17].

The critical radius r_c can be evaluated by differentiating equation 2.9 with respect to radius

$$\frac{d(\Delta G)}{dr} = 8\pi r_c \sigma + 4\pi r_c^2 \Delta G_v = 0 \qquad (2.10)$$

$$r_c = -\frac{2\sigma}{\Delta G_v} \qquad (2.11)$$

The maximum value for the change in free energy which is otherwise known as activation barrier of nucleation (ΔG_{crit}) is given by,

$$\Delta G_{crit} = \frac{4\pi r_c^2 \sigma}{3} \qquad (2.12)$$

Gibb's Thompson equation for the growth of clusters is given by

$$ln\frac{c}{c*} = \ln S = \frac{2\sigma v}{kTr} \qquad (2.13)$$

Where c is the concentration of the cluster of radius r. substituting the value of r in equation 2.12 gives,

$$\Delta G_{crit} = \frac{16\pi\sigma^3 v^2}{3(kTlnS)^2} \qquad (2.14)$$

Rate Determination

The actual mechanism of crystal growth occurs in three different processes,

1. The interface or surface, kinetic process where the atoms and molecules are introduced into the crystal phase through an interface between the crystals and the growth medium.
2. Atoms and molecules in the growth medium are supplied to the growth interface, or crystal surface. This stage is called the volume diffusion process.
3. Latent heat generated at the growth interface during crystallization is removed.

The rate of growth is determined by the rate at which the crystals pass through each of these processes. The process for which the rate of growth is slowest would have highest impact on the overall growth rate [13].

DESIGN AND SYNTHESIS - FLUX METHOD

Roles of Single Crystals and Crystal Growth

A crystal is defined as a solid composed of atoms, ions, or molecules arranged in an orderly three-dimensional pattern that is repeated throughout the entire volume. A single crystal has a continuous crystal lattice and often exhibit anisotropy, which is a property displaying variation in physical properties in different directions along which they are measured. Single crystals have a well-defined natural facet. Quartz, salt, and topaz are a few examples of faceted natural single crystal. The first attempt to grow single crystals in the lab resulted in a stable binary In_2O_3 with nice facets (see Figure 3.1).

Figure 3.1. First grown In_2O_3 (existing) crystal with nice facets.

Although the preferred type of sample for physical properties' measurements in solid-state research is a single crystal, these measurements can also be done using polycrystalline samples. The downside is that the grain boundaries present in the polycrystalline sample tends to scatter light along the voids of these boundaries due to which the crystals are opaque; and also scattering of the electrical currents along the boundaries leads to higher resistivity than single crystals samples [20].

Next comes the question of type of compounds studied by solid-state physicists in recent years; this list comprises an inexhaustible variety of compounds. Transition metal oxides followed by intermetallics were mostly studied in the recent past. Most of the compounds were ternaries and pseudo-ternary compounds. It is worthwhile to note that some of the compounds may already exist and attracted scientists investigating novel properties in the old compounds. Based on this, the single crystal growth activity can be classified into four broad categories.

1. Single crystal growth based on already existing recipe in the literature.
2. Single crystal growth of an existing compound to optimize the size of the crystal to investigate intriguing properties.
3. Single crystal growth on a completely new compound.
4. Single crystal growth on known compound for the first time [20].

Overview of Flux Method

Solid state research utilizes a variety of techniques for single crystal growth. One cannot exactly determine a particular technique that produces single crystals of all compounds. There are instances where the flux method might not produce single crystals of a desired compound, whereas other techniques come in handy for the growth of single crystals of the same compound. It should be noted that single crystals can be grown without using a flux just by solidifying their own melt. This, in fact, yields larger crystals, but reaching temperatures for elements having high

melting points is not achievable with most furnaces available in the lab. Another point of consideration is that the crucible, the vessel holding the chemicals, must also withstand such temperatures. Therefore, the primary role of a flux is to reduce the crystallization temperature. It is a versatile method to produce high quality crystals, the reason being that the growth environment has no significant temperature gradient, and together with slow cooling rates yield crystals with minimal strain and defect. Nevertheless, it is likely that this method may produce an entirely different compound of interesting properties in the event of an exploratory growth procedure. This method is highly suitable for compounds that decompose, convert into another crystalline form or become volatile before reaching the melting point. Flux is a solvent that dissolves solute in the solution. There are several features to be considered for viable flux. They are,

1. A flux must be a material with reasonably low melting point.
2. An appreciable change in solubility with temperature.
3. The metal should have a large variation between its boiling and melting points.
4. It should not react with the crucible.
5. It should be easily extracted from the crucible.
6. Most importantly, they should not form any stable binaries with the reactants.
7. Flux should be available in pure form at low cost.
8. Less toxic [3,20].

Chemical Handling and Equipment for Synthesis

Sealing Station. A typical sealing station has a rotary pump which evacuates the air inside the quartz ampoule and the reactions are sealed using an oxygen-hydrogen torch (see Figure 3.2). Care must be taken such as wearing goggles would help protect the eyes from the intense bright light during the sealing process.

Figure 3.2. Sealing station where the reactions are sealed.

Glovebox. There are certain elements that oxidize when exposed to air. Rare earth elements that were used in the growth of topological semimetals in the lab are not stable to air. In order to prevent these elements from oxidizing, these elements are handled inside the glovebox. A glovebox (see Figure 3.3) is a sealed box where the desired elements could be

handled in a high purity inert atmosphere of nitrogen. It has a pair of gloves on the sides through which the user can insert his/her hands and perform the task as needed.

Figure 3.3. Glovebox to handle elements in a controlled environment.

A series of treatment devices fixed in the glovebox pumps the solvents and oxygen out continuously and they are maintained at a higher pressure than the surrounding air.

Box Furnaces. The next important equipment in line for the crystal growth process is the furnace. The preferred type of furnace in crystal growth process is the box furnace (see Figure 3.4) as it can accommodate more reactions than its counterpart tube furnace, which can typically handle only one reaction at a time.

Figure 3.4. Box furnaces which can withstand 1200°C.

A box furnace has the heating elements fixed on the side walls that would help in uniform distribution of the temperature. The box furnaces available in the lab can withstand 1200°C and are programmable according to the temperature profile employed for the slow cooling process.

Figure 3.5 shows the compartment of a box furnace which can accommodate multiple reactions at a time.

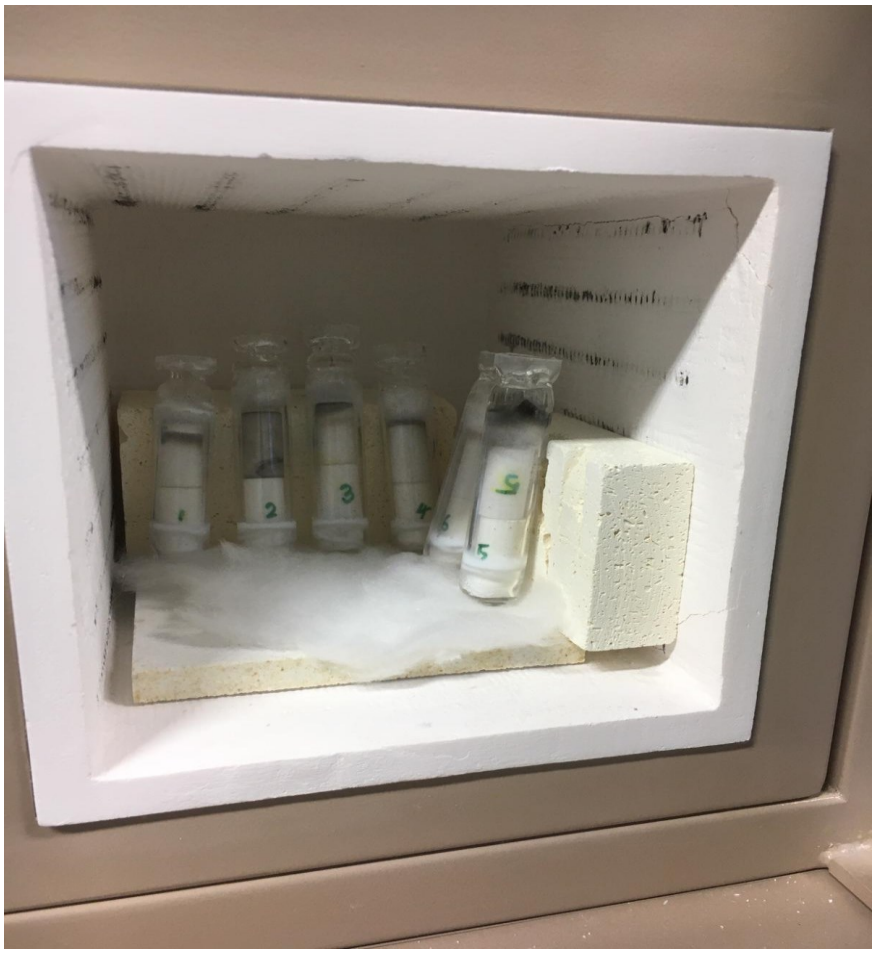

Figure 3.5. The compartment within the box furnace.

Crucibles. Crucibles are needed to hold the starting materials. Crucible materials can be a metal, quartz, graphite, nitrides, or oxides. These materials are chosen based on the starting materials and the flux used. The crucible material can contaminate the crystal which in turn alter the physical properties of the crystal. The key characteristics for crucible selection are that the material should not react with the components of the reaction and that it should withstand high

temperatures [21]. Alumina crucibles (see Figure 3.6), which can withstand temperatures up to 1350°C, were used in this work.

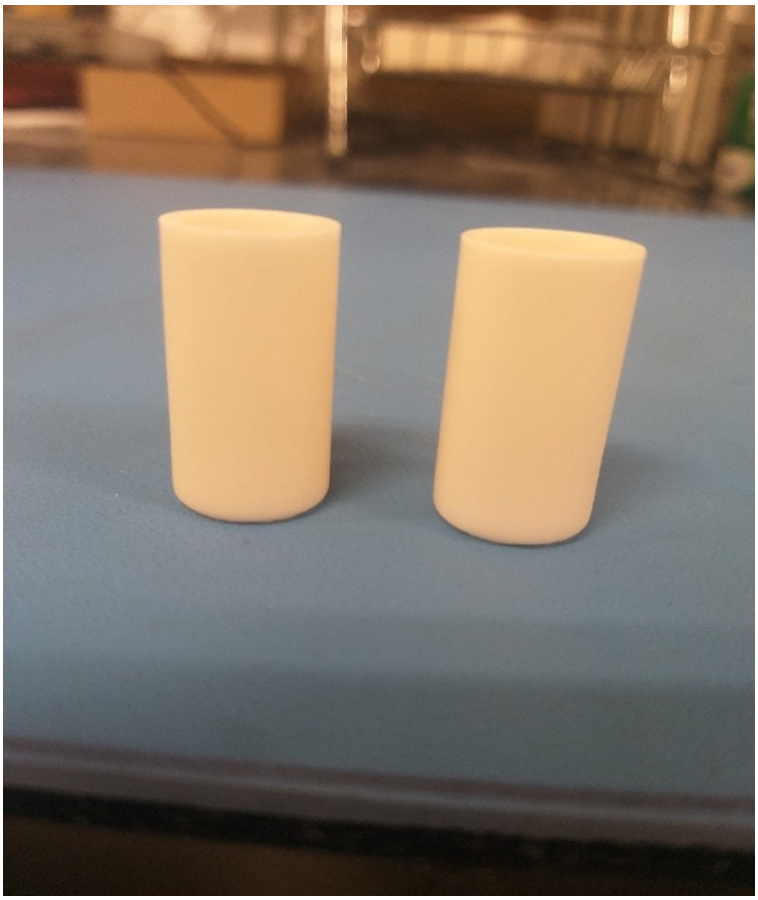

Figure 3.6. Alumina crucibles for holding the reaction.

Centrifuge. The residual flux can be removed from the grown crystals in two different ways. One method could be if water or aqueous reagent dissolves the flux without attacking the crystals. The other method could be to centrifuge the reactions. For this, the quartz ampoule is removed from the furnace quickly, inverted, and centrifuged for a few seconds while the reaction is still molten. The flux gets collected in the catch crucible. Figure 3.7 displays the centrifuges available in the lab.

Figure 3.7. Centrifuge to remove excess flux.

GROWTH OF $SmMnBi_2$

Outline of Growth Process Specific to $SmMnBi_2$

Materials with outstanding physical properties can be synthesized through different combination of chemical constituents and one of such types is ternary intermetallics. The goal here is to synthesize ternary intermetallics that could be a topological semimetal candidate utilizing flux method. With this focus, two different metallic fluxes such as bismuth and antimony were employed in the growth process. Initial trials were attempted to grow already reported compound such as $BaMnBi_2$ and $BaMnSb_2$. This served as an exploratory trial to check if it could be resynthesized using flux method and showed that the method was successful. Following this, systematic growth was undertaken with various combinations of transition metals and rare earth elements. Bismuth and antimony are the two metallic fluxes used with a variety of different combinations of first elements (Ba, Yb, Tm, Sm) and second elements (Mn, Co, Cr, V, Mo) that eventually yielded single crystals of $SmMnBi_2$, that could be a potential topological semimetal. Different steps involved in the growth process of the layered transition metal pnictides are enumerated here. First and foremost, the required length of silica tube is measured, cut and sealed on the bottom edge. The closed end should be a round or flat bottomed to prevent cracking during the growth process. The starting chemicals are weighed and loaded into alumina crucibles taking care to minimize contamination. In this process, chemicals with low melting points are placed on top of the chemicals with high melting point in the crucible, the reason being the low melting chemicals melt first and engulf other chemicals as the reaction progresses [20].

Interpretation of Different Growth Phases in $SmMnBi_2$

Knowledge of phase diagrams is essential for solid-state research. Phase diagrams are plots that displays the phase transformation taking place under various conditions of composition, pressure, and temperature. Phase diagrams can be used to gather relevant information such as cooling rate, starting composition, and temperature profile. A phase diagram depicts the different states of matter as a function of temperature and composition. Phase diagrams are usually constructed with a constant pressure of one atmosphere [22]. Based on this information, a temperature profile is generated taking care to avoid secondary phases in the melt, to facilitate congruent melting, and to stimulate conditions favoring a large single crystal growth.

Figure 4.1 shows a binary phase diagram of Bi-Sm. Consider a Bi:Sm mixture at a concentration of 10:1 atomic percent (blue arrow in Figure 4.1). At high temperatures, the mixture is in a liquid phase. On cooling, the process of solidification starts when the temperature reaches the liquidus line at approximately 700°C.

According to the phase diagram, further cooling of the melt enters a solid-liquid zone expecting to yield a combination of liquid phase and solid phase of Bi_2Sm. Conversely, the growth process produced stable binaries of BiSm, with EDS results confirming a composition of 50:50 atomic percent.

It is worth mentioning that at high temperatures the growth conditions do favor the formation of thermodynamically stable BiSm, which has bonds that are difficult to break and to facilitate the formation of Bi_2Sm [3]. One way to overcome the hurdle of forming a stable binary is to centrifuge the reaction at still higher temperature, well above the liquidus line, say around 800°C. The downside may be less growth time that may yield small sized crystals.

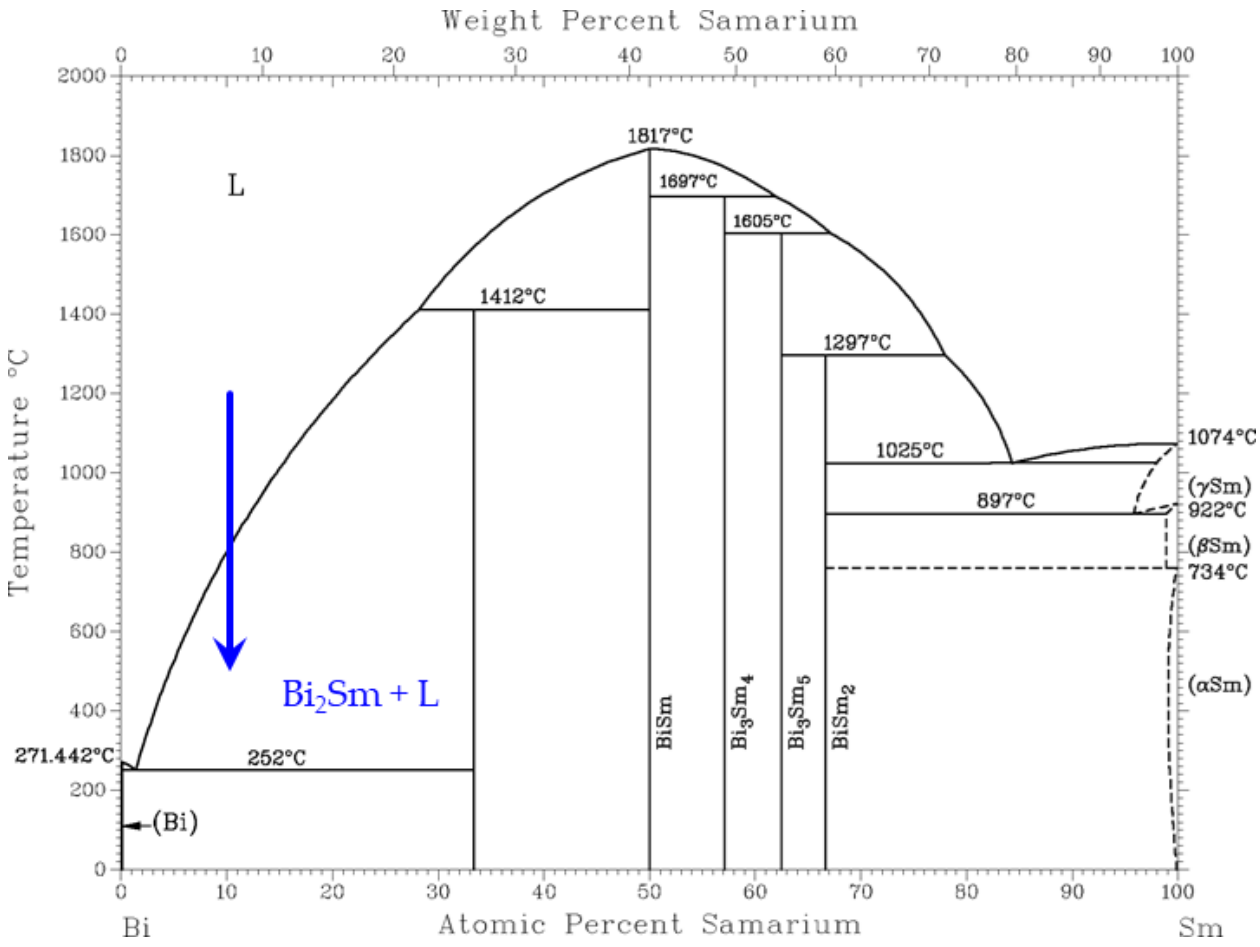

Figure 4.1. Bi-Sm binary phase diagram.

Figure 4.2 represents the Bi-Mn binary phase diagram. The phase diagram indicates that on cooling the melt having Bi:Mn composition of 10:1 atomic percent (blue arrow), the solidification starts when it touches the liquidus line at 355°C where there are chances of formation of the stable binary BiMn. But the reaction is set to be centrifuged at 500°C, considering involvement of other element and this prevents the process entering into the stable binary phase and eventually facilitate the formation of a ternary intermetallic compound with Sm.

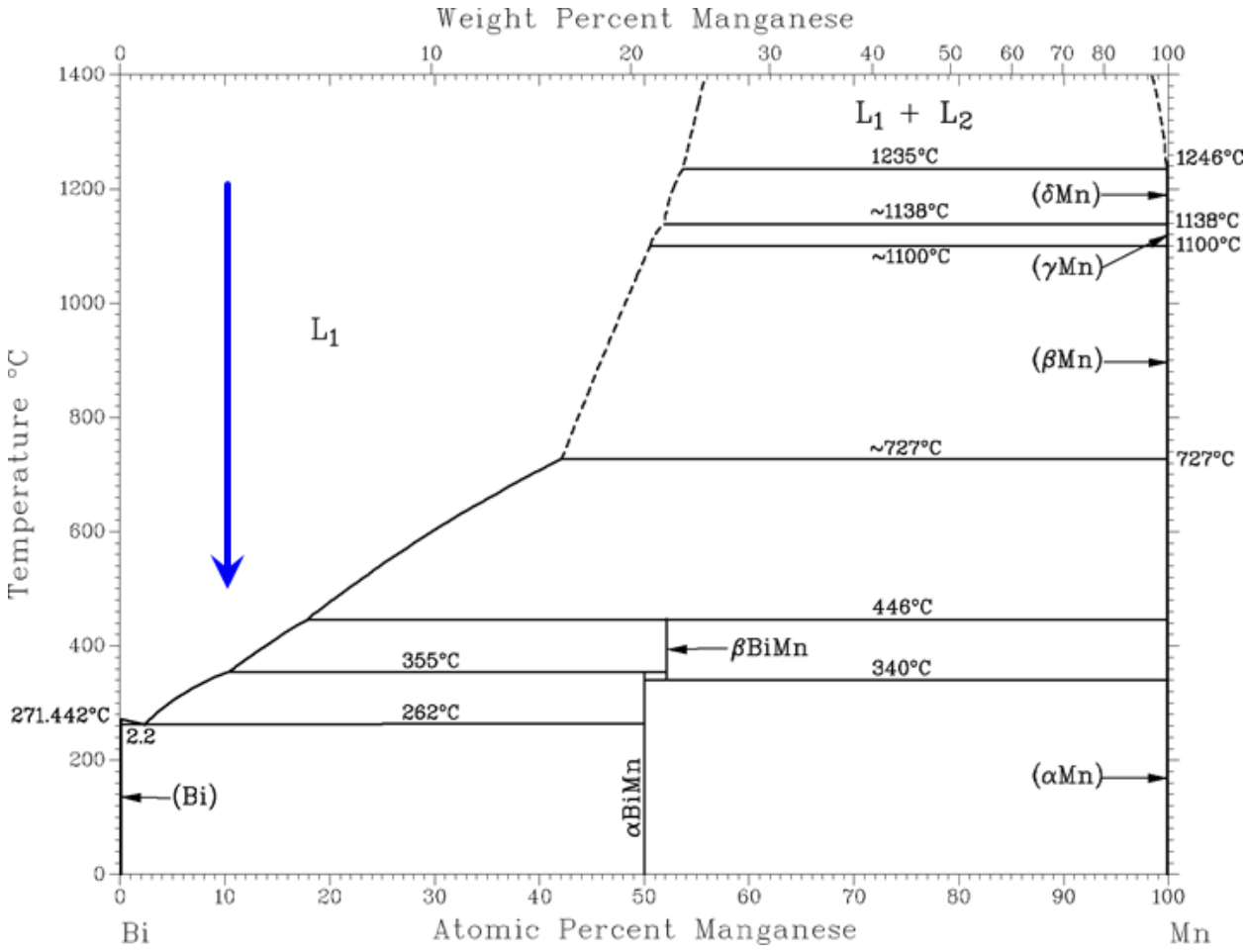

Figure 4.2. Bi-Mn binary phase diagram.

Consider the composition of the melt at 50:50 ratio of Mn:Sm (blue arrow in Figure 4.3). At high temperatures, a single liquid phase exists. On cooling, the solidification begins when the temperature touches the liquidus curve around 950°C, producing, according to the phase diagram, $Mn_{23}Sm_6$. On further cooling to a temperature of 930°C, one enters a region which theoretically predicts the formation of Mn_2Sm (dashed lines), until just below 800°C, at which point solid Sm is produced. However, none of these compounds were discovered in the Bi-rich growth.

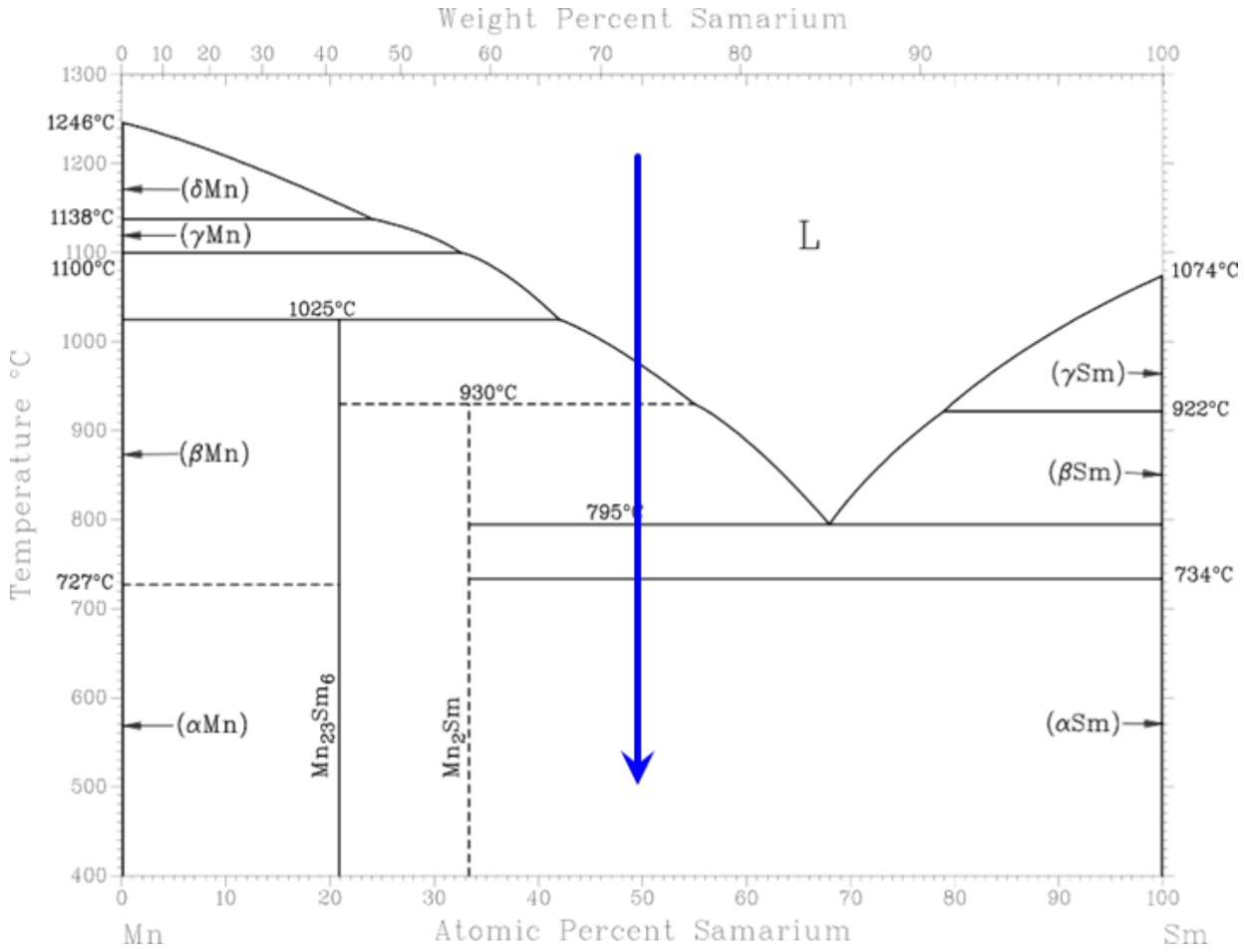

Figure 4.3. Mn-Sm binary phase diagram.

Changing the ratio to 20:1 or higher would mean that at a 500-600°C centrifugation, these two elements would not reach a liquidus line, therefore hindering any formation of binaries.

A number of things can be interpreted from the study of the three binary phase diagrams. Allowing the reaction to cool to 500°C with a 10:1 Bi:Sm ratio forms a BiSm binary formation, therefore “wasting” some of the material into this undesired compound.

By centrifuging at 800°C instead of 500°C, the 10:1 Bi:Sm ratio does not enter the solid-liquid region. The drawback is a shorter temperature range allowed for growth, possibly not even reaching the temperature at which $SmMnBi_2$ grows (at this point, this temperature is unknown).

None of the expected and predicted Mn-Sm binaries were produced in the bismuth-rich environment. This indicated that the molten bath of bismuth facilitates growths of Bi-containing compounds. It is possible that Mn-Sm binaries formed but remained in the flux.

By changing the Mn:Sm ratio to 32:68, a eutectic allows these two compounds to remain in liquid state until 795°C. Centrifugation at 800°C then would at least hinder any possible Mn-Sm binaries to form. In combination with the point mentioned above (larger amounts of Bi), this could mean greater yield of the desired product $SmMnBi_2$.

Fabrication of $SmMnBi_2$

Starting materials of manganese and samarium were measured and inserted into an alumina crucible, followed by an amount of bismuth to reach the desired 10:1:1 Bi:Sm:Mn molar ratio. The crucible was then inserted into a quartz tube, followed by a second alumina crucible, inserted upside down on top of the first crucible. This second crucible was filled with quartz wool (fused silica fibers) to act as a catch crucible to collect the excess flux during the decantation process. The preparation took place in an inert atmosphere in the glovebox to hinder oxidation of samarium and to also ensure that the crucibles and the quartz wool did not trap any air or moisture. The quartz tube was then evacuated of its atmosphere and sealed while in vacuum using the blow torch to melt and collapse the quartz above the crucible pair. The sealed ampoule was then placed in a nearly upright position inside the box furnace. The ampoule was heated up to 1100°C at a rate of 100°C per hour and held at this temperature for about 10 hours,

followed by slow-cooling at a rate of 5°C per hour until 500°C (see Figure 4.4 for the temperature profile).

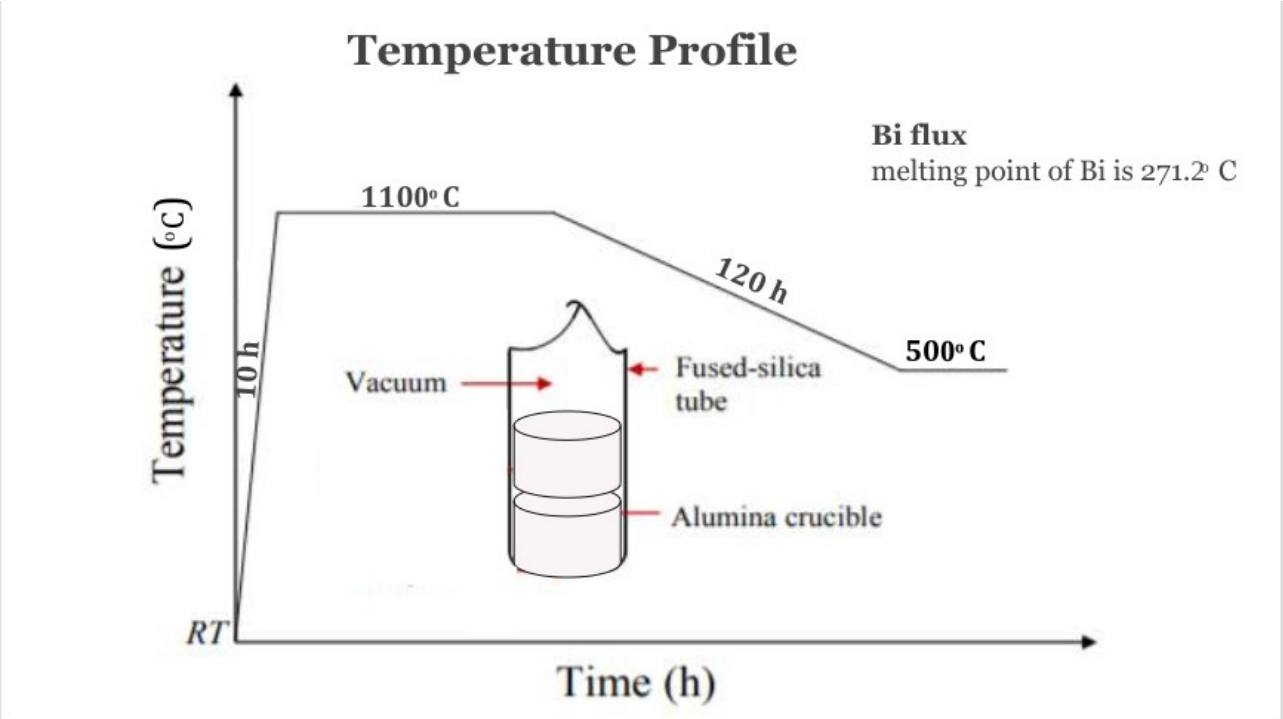

Figure 4.4. Temperature profile for Bi flux.

At that temperature, the quart ampoule was rapidly removed from the furnace and centrifuged to isolate the crystals from the flux. The centrifugation was allowed to proceed until the flux solidified. The process is illustrated in Figure 4.5.

After the quartz ampoules cooled enough to allow for handling, they were broken apart and the crystals were harvested. The product appeared as thin, plate-like crystals of dark metallic luster.

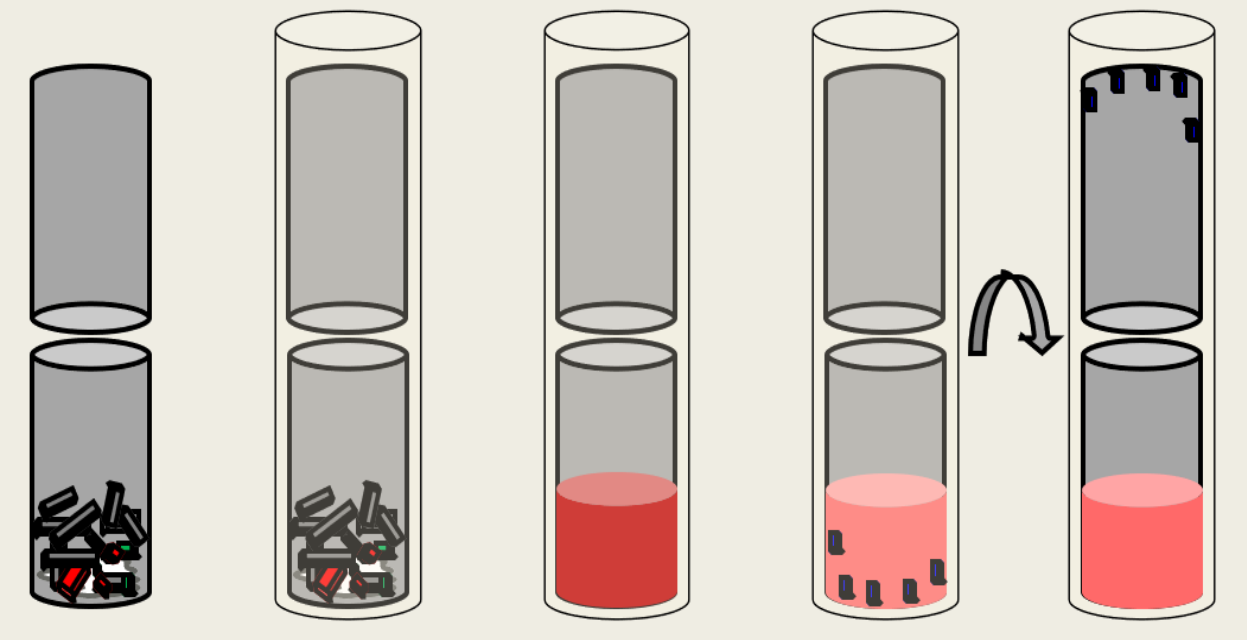

Figure 4.5. Step by step illustration of the flux method.

RESULTS AND DISCUSSION

Scanning Electron Microscopy/Energy Dispersive Spectroscopy

Scanning electron microscopy (SEM) allows materials to be examined at extremely high magnifications and also produces images of high resolution. Electrons generated from an electron gun interact with the surface of the specimen and generate many low energy secondary electrons, which are detected to produce image based on the topography of the surface. The working principle is shown in Figure 5.1.

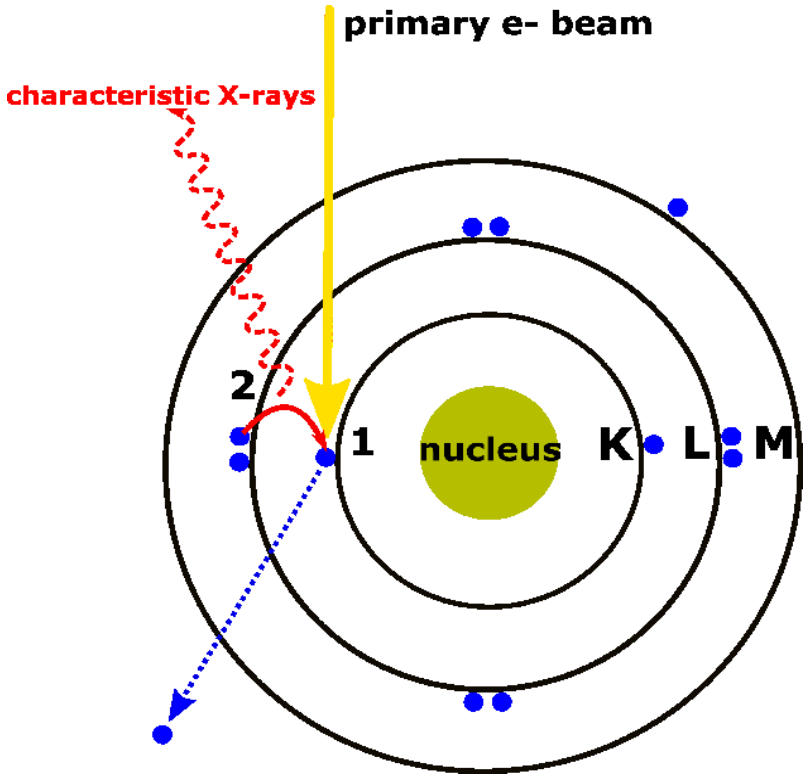

Figure 5.1. EDS working principle.

The secondary electron detector (SED) and the backscattered electron detectors are the two most commonly used detector to produce images. Energy dispersive spectroscopy (EDS)

can be used to find the chemical composition of the material with atomic number greater than 3. When the electron beam hits the inner shell of an atom, it knocks off an electron from the shell, creating a vacancy or an electron hole. This vacancy is filled as the electron moves from the outer higher-energy to the inner lower-energy shell of the atom. This energy difference can be released in the form of an X-ray. The x-ray detector gathers this information and converts it into useful information. Figure 5.2 shows the SEM image of one of the $SmMnBi_2$ crystals taken under the SED mode under high magnification. This image substantiates the existence of well-defined facets with nice edges. The droplets on the crystals are bismuth (flux remnants).

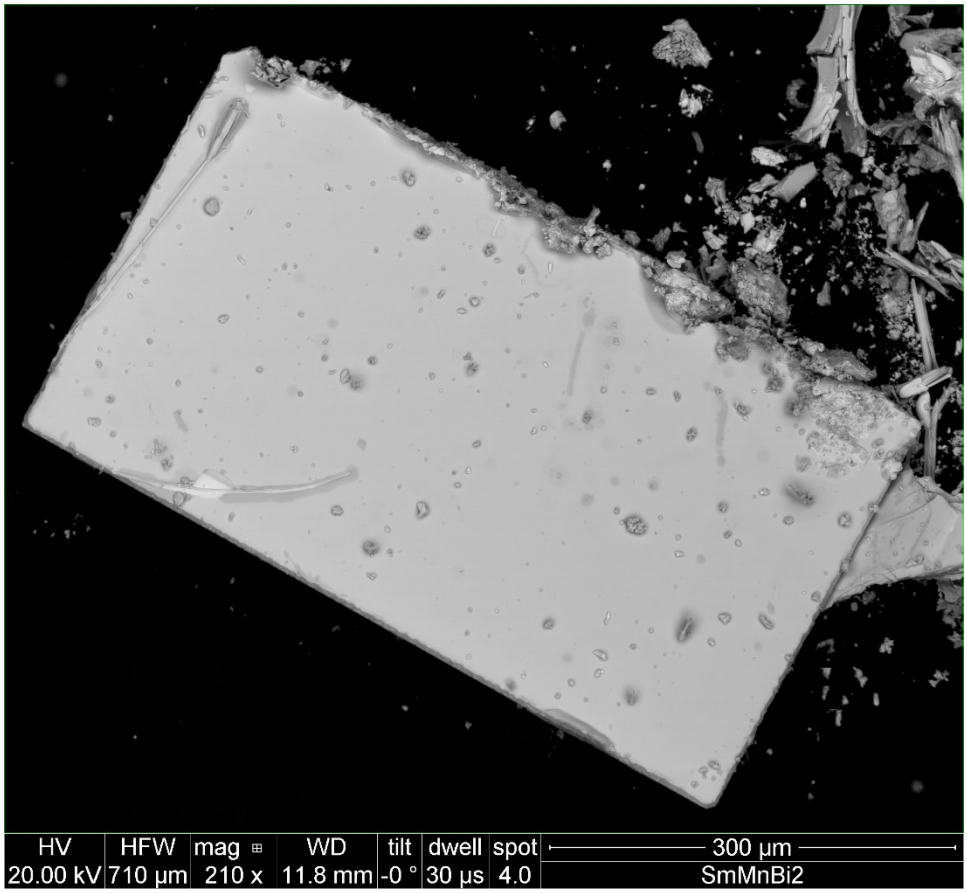

Figure 5.2. Secondary electron image of $SmMnBi_2$.

Figure 5.3 depicts the EDS micrograph of the layered manganese pnictide $SmMnBi_2$. The presence of all three elements is confirmed with samarium Lα at 5.63 eV and Mα at 1.08 eV, manganese Kα at 5.90 eV and Lα at 0.64 eV, and bismuth Lα at 10.84 eV and Mα at 2.42 eV. A variety of alpha-2 and beta lines are also observed.

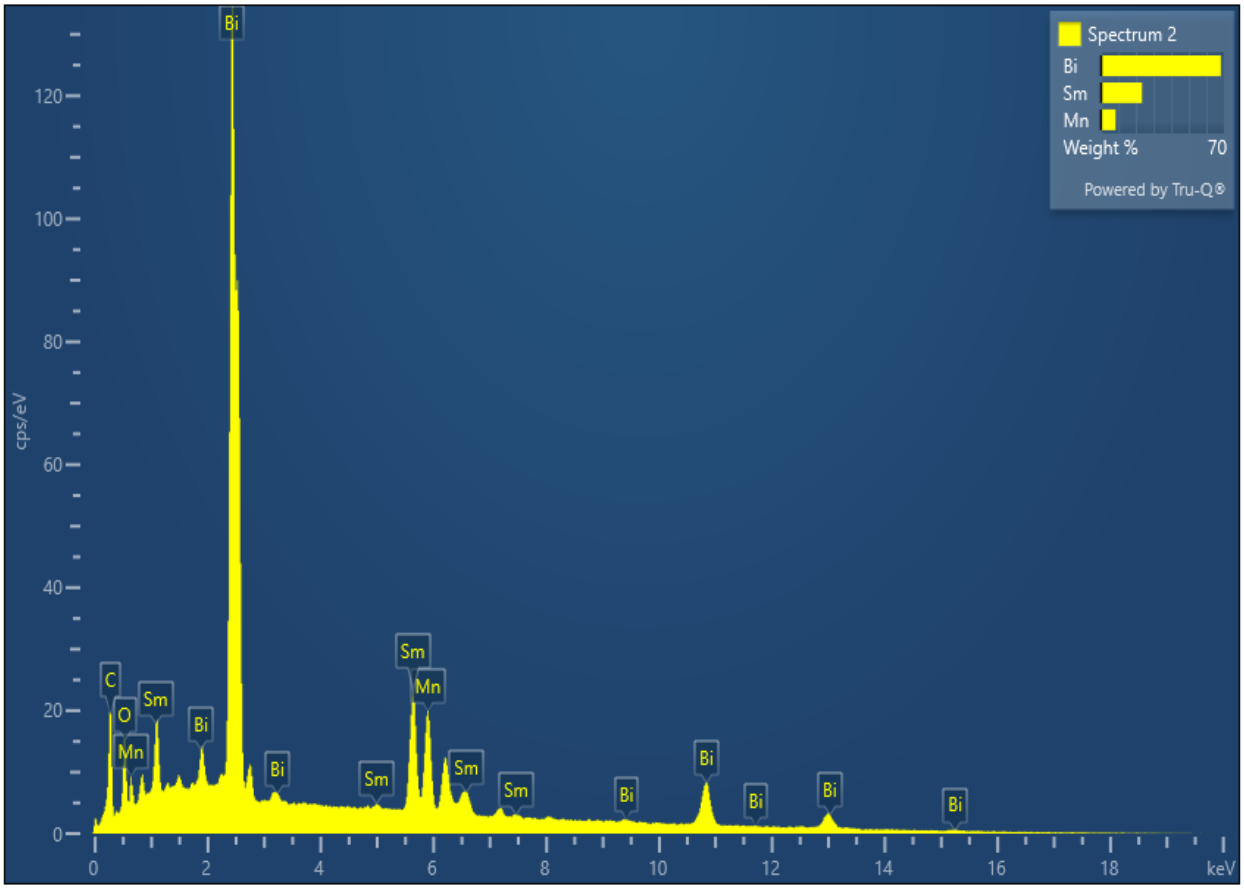

Figure 5.3. EDS micrograph of $SmMnBi_2$.

The elemental composition of $SmMnBi_2$ was confirmed by EDS to within a 1–2 atomic percent error. This was performed on various specimens as well as at different sites on the same specimen. The obtained results are summarized in Table 5.1 as given by the analysis software.

Table 5.1. Relative composition in atomic% of Mn, Sm, and Bi.

Element	Atomic %							
Sm	24.23	24.34	23.68	23.61	24.57	24.28	24.69	25.16
Mn	24.56	25.31	24.31	23.72	24.05	24.33	23.98	24.77
Bi	51.21	50.35	52.01	52.67	51.38	51.39	51.32	50.06

Crystal Structure Determination – Single Crystal XRD

X-ray diffraction is based on the constructive interference of monochromatic x-rays and crystalline sample. When conditions satisfy Bragg's law ($n\lambda=2d\sin\theta$), the interaction between the sample and the incident ray produces diffraction pattern that is used to detect the structure of the compound. Figure 5.4 represents the schematic of single crystal x-ray diffractometer that utilizes 4-circle goniometers. Each circle represents four angles (2θ, χ, φ, and Ω) that shows the relationship between the incident ray, detector, and crystal lattice.

The crystal structure of the newly grown compound $SmMnBi_2$ is presented here. The data was collected at the University of Oklahoma, utilizing a user-service. A black block-shaped crystal of dimensions 0.016 x 0.054 x 0.064 mm was selected for the structural analysis. Intensity data were collected using a D8 Quest κ-geometry diffractometer with a Bruker Photon II CMOS area detector and an Incoatec Iμs microfocus Mo Kα source (λ = 0.71073 Å).

The sample was cooled to 102(2) K. Cell parameters were determined from a least-squares fit of 2313 peaks in the range $4.63° < \theta < 33.66°$. A total of 5072 data were measured in the range $3.958° < \theta < 33.711°$ using ϕ and ω oscillation frames. The data were corrected for absorption by the empirical method. The data were merged to form a set of 292 independent reflections with R(int) = 0.0784 and a coverage of 99.3%.

The tetragonal space group *I*4/*mmm* was determined by systematic absences and statistical tests and verified by subsequent refinement. The structure was solved by dual-space methods and refined by full-matrix least-squares methods on F^2, both at the University of Oklahoma and at Missouri State University.

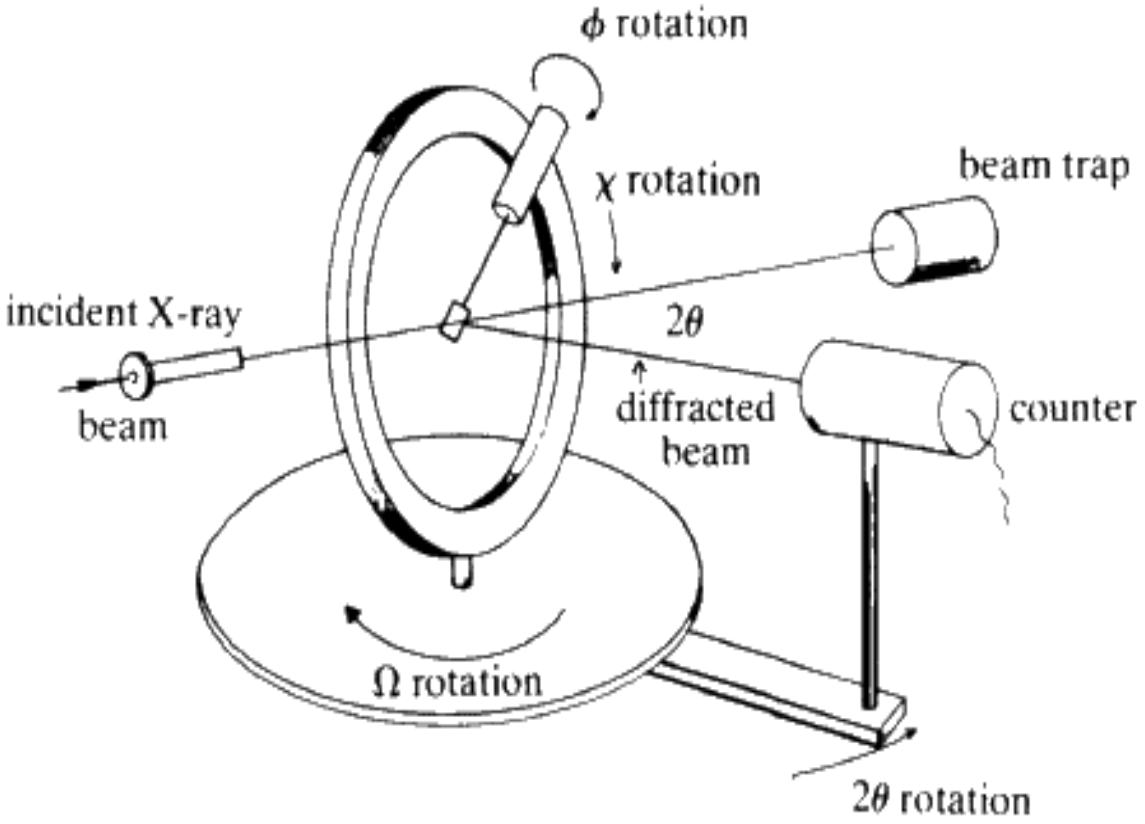

Figure 5.4. Schematic of single crystal x-ray diffraction.

All atoms were refined with anisotropic displacement parameters. A total of 13 parameters were refined against 0 restraints and 292 reflections to yield wR(F^2) = 0.0738 and R(F) = 0.0440. The refinement parameters are summarized in Table 5.2. $SmMnBi_2$ crystallizes in the tetragonal centrosymmetric space group *I*4/*mmm* (Z = 4) with unit cell dimensions a = 4.5054(4) Å and c = 20.591(2) Å, and the atomic positions are summarized in Table 5.3.

Table 5.2. Crystallographic parameters of $SmMnBi_2$

Compound	$SmMnBi_2$
Molecular weight	623.29 g/mol
Space group	*I*4/*mmm* (#139)
A	4.5054(4) Å
C	20.591(2) Å
Z	4
Volume	417.98(8) $Å^3$
ρ_{calc}	9.904 g/cm^3
Data collection range	$3.958° < \theta < 33.711°$
Collected reflections	5072
Independent reflections	292
Refined parameters	16
Restraints	0
R_1	0.0440
wR_2	0.0738
Goodness-of-fit against F^2	1.0961

Table 5.3. Atomic positions of $SmMnBi_2$.

Atom	Site	*x*	*y*	*z*	U_{eq} ($Å^2$)
Sm	4e	½	½	0.62275	0.015(1)
Mn	4c	0	½	½	0.017(4)
Bi1	4d	0	½	¾	0.015(1)
Bi2	4e	0	0	0.59612	0.014(1)

A generated powder x-ray diffraction pattern from the final single crystal structure is displayed in Figure 5.5.

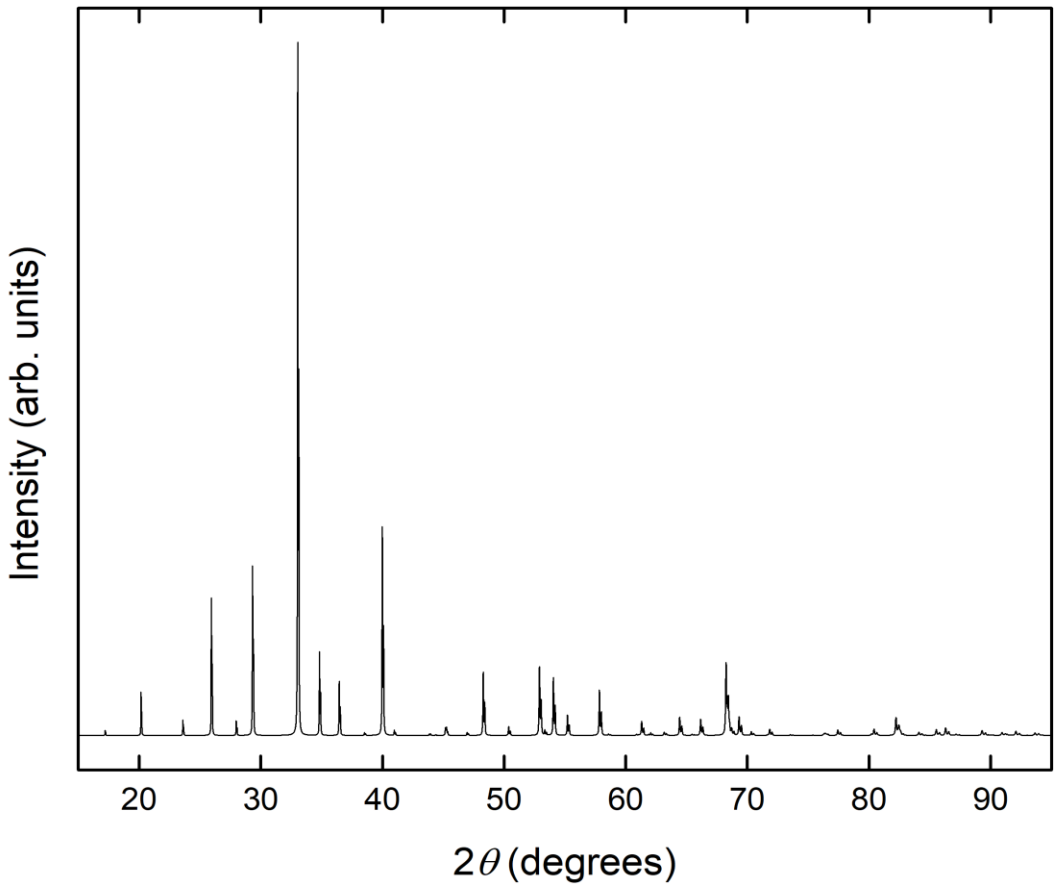

Figure 5.5. Generated powder diffraction pattern for $SmMnBi_2$ from the single crystal structure.

$SmMnBi_2$ is built up from three layers (see Figure 5.6): puckered rock-salt-like SmBi slabs (comprising the Bi2 site), square Mn-nets, and square Bi-nets (comprising the Bi1 site). The Mn- and Bi-nets alternate along the *c*-axis, stacked coincidentally (…A-A… stacking). The Mn-Mn and Bi-Bi intraplanar distances are both ~3.19 Å, average for manganese but relatively short for bismuth. The SmBi slabs is stacked between the Mn- and Bi-nets along the *c*-axis,

following an …A-A-B-B-A-A… stacking sequence. The puckering of the SmBi slabs is always with the rare earth element towards the Bi-net.

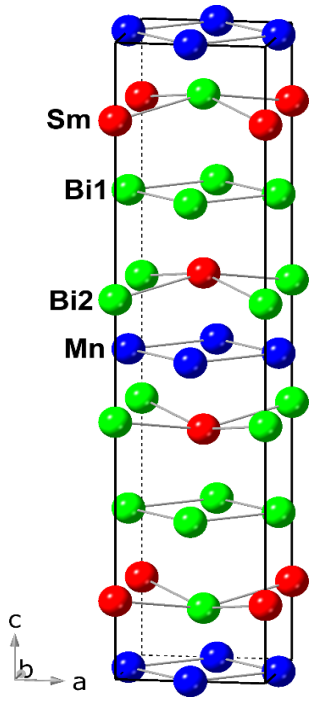

Figure 5.6. Unit cell of $SmMnBi_2$.

Structure Analysis - $SmMnBi_2$

At first, it was believed that $SmMnBi_2$ would be fully isostructural with either the existing Dirac semimetal $EuMnBi_2$ [23–26] or the Weyl semimetal $YbMnBi_2$ [9,27–32]. Comparing space groups and lattice parameters, it looks as if $SmMnBi_2$ is isostructural to $EuMnBi_2$ which also crystallizes in $I4/mmm$ and with similar lattice parameters. This makes sense and is expected: Sm and Eu are adjacent to each other in the periodic table of elements and differ very little in ionic size. $YbMnBi_2$, on the other hand, crystallizes in $P4/nmm$ ($Z = 2$) and with a *c*-axis closer to half of that of $SmMnBi_2$ (see Table 5.4) [9,27].

Table 5.4 Comparison of space groups and lattice parameters of (Sm,Eu,Yb)$MnBi_2$. The parameters for $SmMnBi_2$ are from this work. Since no CIF exists for $YbMnBi_2$, its parameters were taken directly from the reference.

	$SmBiMn_2$	$EuMnBi_2$ [23]	$YbMnBi_2$ [27]
Space group	*I*4/*mmm*	*I*4/*mmm*	*P*4/*nmm*
a (Å)	4.5054(4)	4.5342(6)	4.488(2)
c (Å)	20.591(2)	22.427(4)	10.826(2)
Z	4	4	2

Figure 5.7 compares the unit cell of $SmMnBi_2$ to that of the structurally related topological compounds $EuMnBi_2$ and $YbMnBi_2$. No CIF exists for $YbMnBi_2$, hence, this structure is constructed using a CIF for the fully isostructural $CaMnBi_2$ [33].

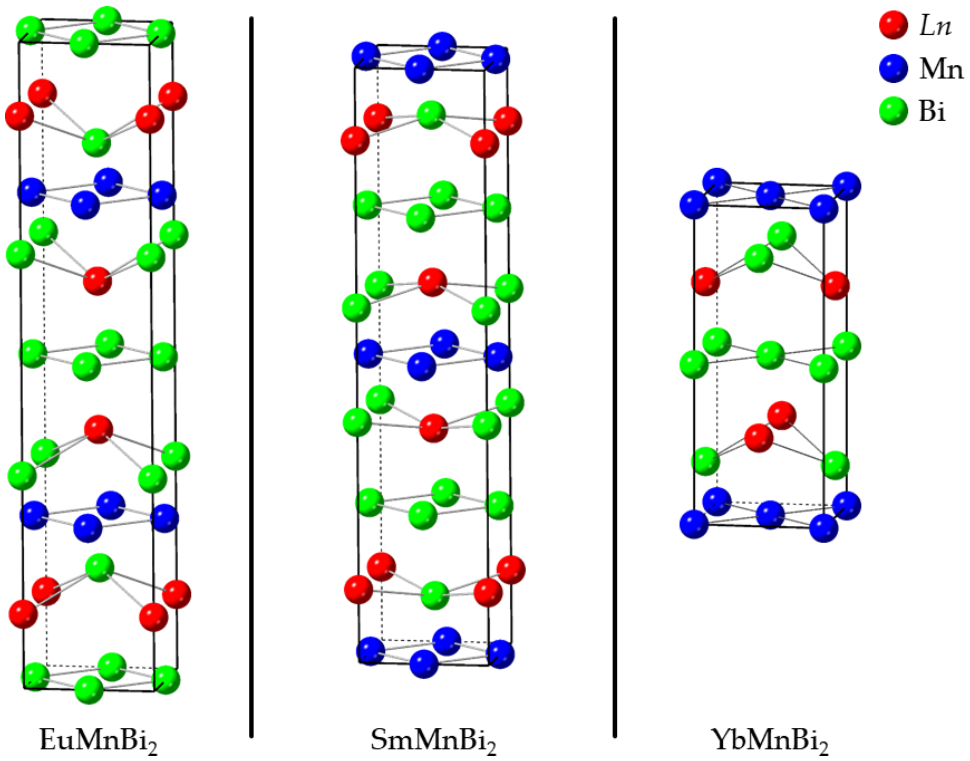

Figure 5.7. Comparison of crystal structure of $SmMnBi_2$ (center) with the other structurally related topological compounds: $EuMnBi_2$ (left) and $YbMnBi_2$ (right).

On a closer comparison between the structures, it is obvious that, besides the similiarities, several discrepancies exist to conclude that $SmMnBi_2$ and $EuMnBi_2$ are not completely isostructural, and not isostructural with $YbMnBi_2$. Extended crystal structures are in Figure 5.8.

The first discrepancy is the obvious space group and lattice parameters. It has already been mentioned that $YbMnBi_2$ crystallizes in *P*4/*nmm* while both $SmMnBi_2$ and $EuMnBi_2$ crystallize in *I*4/*mmm*. Even though the rare earths samarium and europium are adjacent and have near-identical ionic size with Sm slightly larger, the difference in the unit cell dimensions of $SmMnBi_2$ and $EuMnBi_2$ is remarkable: $SmMnBi_2$ is considerably smaller than $EuMnBi_2$. The *c*-axis of $EuMnBi_2$ is almost 9 % longer than the one in $SmMnBi_2$ (the *a*-axis is about 0.64% longer). While this may have very small effects on any intraplanar interactions within the nets, it may introduce interplanar interactions.

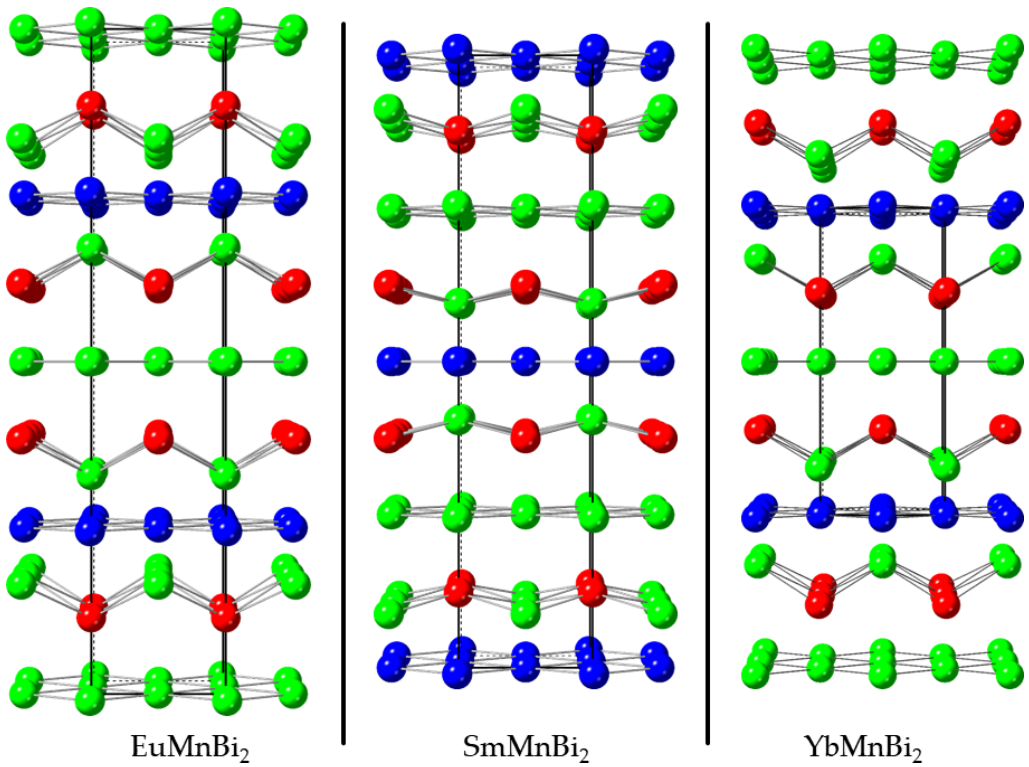

Figure 5.8. Extended crystal structures of (Eu,Sm,Yb)$MnBi_2$.

Another discrepancy is the obvious centering: while $EuMnBi_2$ has a mirror symmetry along its *c*-axis at the Bi-net, $SmMnBi_2$ has its mirror symmetry along its *c*-axis at the Mn-net. Transforming the $SmMnBi_2$ unit cell one-half along the *c*-axis would put a Bi-net in the center, however, the structure would also lose its mirror symmetry along that axis. While the buckling of the *Ln*Bi slab is towards the Bi-net in all three structures, the angle is considerably larger in $SmMnBi_2$: approximately 160.5° for $SmMnBi_2$ and approximately 136.9° for $EuMnBi_2$, despite the near-identical ionic size of Sm and Eu. Since no Crystallographic Information File (CIF) exists for $YbMnBi_2$, no bond length or bond angle comparison can be made with it.

The …A-A-B-B-A-A… stacking of the SmBi rock-salt-like slab in $SmMnBi_2$ is coincident with respect to the Mn-net (i.e., the rare earth is stacked coincidentally above and below the Mn-net). This gives rise to an octahedral arrangement between the Sm and the Mn-net with 3.386 Å bond length (see Figure 5.9). While $EuMnBi_2$ also displays …A-A-B-B-A-A… of its EuBi slab, it is stacked coincidentally above and below the Bi-net, therefore having no octahedral arrangement between the Eu and the Mn-net. The bond length is also longer: 3.786 Å. The different stacking in $SmMnBi_2$ may therefore give rise to interplanar interactions between the Mn-net and the rare earth above and below it, which will likely be enhanced by the smaller unit cell of $SmMnBi_2$. The stacking of the YbBi slab in $YbMnBi_2$ follows an …A-B-A-B-A… stacking sequence, i.e., it is staggered. This gives rise to the same arrangement between Yb and the Mn-net as in $EuMnBi_2$.

Although these discrepancies are noteworthy, all three compounds exhibit similarities which likley guides their topological physics. In fact, all these structures are part of a larger family of (*AE*,*RE*)$Mn(Bi,Sb)_2$ structures [34,35]. Due to the strong spin orbit in the heavy bismuth, the square Bi-net opens up the gap at the Dirac nodes, leading to massive fermions

[35,36], and these structures exhibit highly anisotropic Dirac fermions [36]. In addition, the staggered geometry with respect to the Bi-net, as seen in the *P*4/*nmm* structures such as $YbMnBi_2$, protects more Dirac crossings than the coincident geometry [9].

In general in this family of compounds, coincident ordering leads to the Dirac band topology while a staggered ordering leads to the nodal-line band topology [34]. Although $SmMnBi_2$ has a different atomic arrangement, it, too, is expected to display these features since they are associated with the square Bi-net, which is prevalent in all the different compounds in this family of materials.

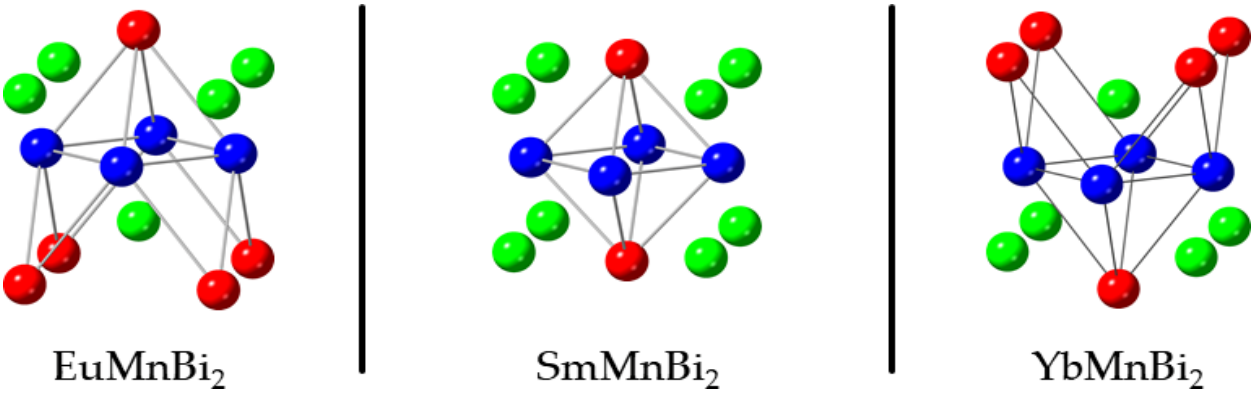

Figure 5.9. The rare earth arrangement around the Mn-net for the three structures.

In both $EuMnBi_2$ and $YbMnBi_2$, antiferromagnetic order has been observed and is due to the Mn-centered, edge-shared $MnBi_4$ tetrahedra [23,27]. $SmMnBi_2$, on the other hand, does not have any $MnBi_4$ tetrahedra due to the coincident stacking of the SmBi slabs above and below the Mn-net (see Figure 5.10 for a focus on the local atomic environment around Mn in all three structures).

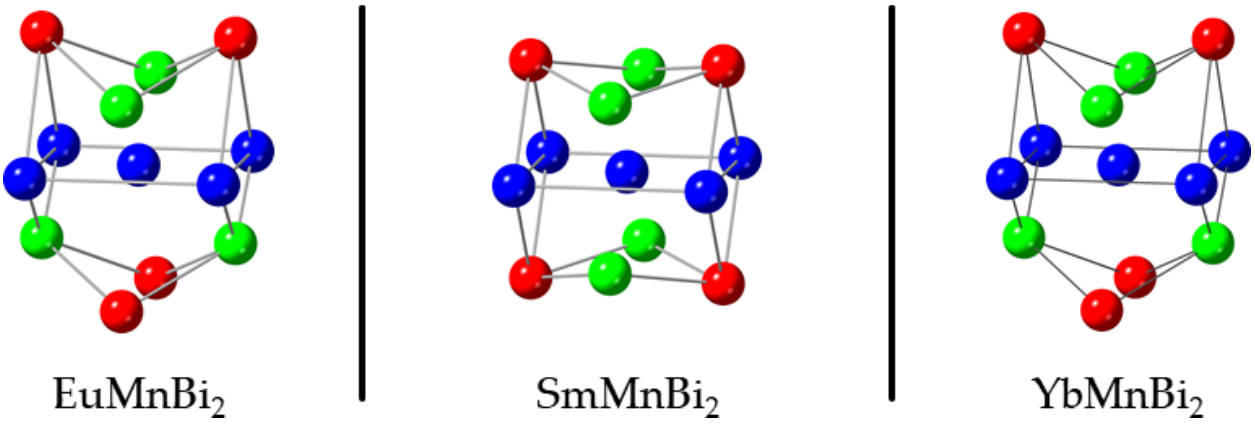

Figure 5.10. Atomic environments around the Mn in the (Eu,Sm,Yb)$MnBi_2$ structures.

It is obvious that the $MnBi_4$ coordination is not tetrahedral in $SmMnBi_2$, but rather Mn-centered, edge-shared square planar (see Figure 5.11). Absence of ligands on the *z*-axis in a square planar complex lowers the electronic repulsion compared to a tetrahedral complex and therefore square planar complexes are nearly always low-spin that would make $SmMnBi_2$ diamagnetic [37,38]. However, as mentioned earlier, the different arrangement with respect to the Mn-net (Figure 5.9) may give rise to more complicated interactions.

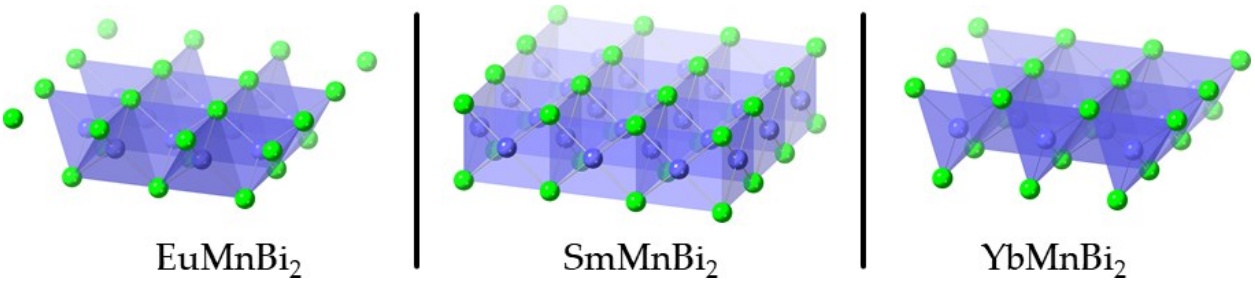

Figure 5.11. $MnBi_4$ coordination in (Eu,Sm,Yb)$MnBi_2$ Both $EuMnBi_2$ and $YbMnBi_2$ display tetrahedral coordination (left, right), while $SmMnBi_2$ displays square planar coordination (center).

CONCLUSION AND FUTURE WORK

A flux method was utilized to synthesize single crystals of the previously unknown $SmMnBi_2$, a potential Dirac or Weyl topological semimetal candidate. The crystal structure was solved using single crystal x-ray diffraction and the structural properties were studied and compared against existing topological compound within the same structural family. Both structural similarities and differences exist between $SmMnBi_2$ and already reported compounds $YbMnBi_2$ and $EuMnBi_2$. The presence of a square Bi-net in the unit cell, a host for Dirac fermions in both $EuMnBi_2$ and $YbMnBi_2$, indicates that $SmMnBi_2$, too, may be a Dirac semimetal. The doubling of the unit cell when compared to $YbMnBi_2$ may be attributed to the staggered coordination of the rare earth Sm on both sides of the Bi-net. Further, since $SmMnBi_2$ exhibits square planar coordination around its antiferromagnetic Mn leads to the prediction that this material could be diamagnetic as electrons are completely paired up at the lower energy levels. This is in contrast to both $EuMnBi_2$ and $YbMnBi_2$ which exhibit tetrahedral coordination.

Three-dimensional topological materials are usually characterized by the nature of non-trivial bulk and surface electronic states as well as requires probing of electromagnetic properties of the material. The bulk and surface electronic state properties are being explored using Angle Resolved Photoemission Spectroscopy (ARPES) [39] in collaboration with Princeton University. ARPES has become indispensable experimental tool to explore topological materials based on photoelectric effect. In ARPES, the sample under investigation is placed under ultrahigh vacuum placed next to an electron analyzer. The material absorbs the photons and emits electrons. These photoelectrons are collected and analyzed with respect to the kinetic energy and emission angle using a spectrometer as illustrated in Figure 6.1.

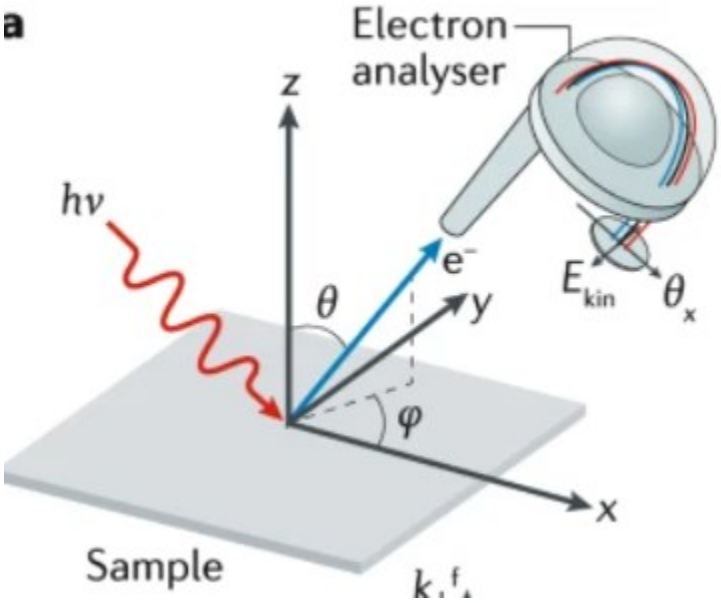

Figure 6.1. Principles of ARPES [39].

Further, electrical and magnetic properties are yet to be determined. Specifically, magnetization measurements need to be done to unearth the magnetic properties (if any) of this new compound, as well as band structure calculations to determine the density-of-states. One primary goal in the future would be to increase the yield of $SmMnBi_2$ by altering the temperature profile that could prevent binary formation. Larger, and cleaner crystals are crucial both for ARPES measurements as well as magnetization measurements. The earlier attempts to increase the yield of $SmMnBi_2$ by varying the proportions of the ingredients resulted in Mn-rich ternary compounds $Sm_{(2,3,4)}Mn_{13}Bi_{(5,4,3)}$, an unknown family of materials. In addition, antimony flux is being explored to further expand this family of topological semimetals.

REFERENCES

[1] L. M. Schoop, X. Dai, R. J. Cava, and R. Ilan, Special topic on topological semimetals–new directions, APL Mater. **8**, 030401 (2020).

[2] S. Sarkar and S. Peter, Single crystal growth of Europium and Ytterbium based intermetallic compounds using metal flux technique, J. Chem. Sci. **124**, 1385 (2013).

[3] M. G. Kanatzidis, R. Pöttgen, and W. Jeitschko, The metal flux: a preparative tool for the exploration of intermetallic compounds, Angew. Chem. Int. Ed. **44**, 6996 (2005).

[4] L. Schoop, F. Pielnhofer, and B. Lotsch, Chemical principles of topological semimetals, Chem. Mater. **30**, 3155 (2018).

[5] A. Burkov, Topological semimetals, Nat. Mater. **15**, 1145 (2016).

[6] *Editorial*, After a Weyl, Nat. Phys. **11**, 697 (2015).

[7] B. Yan and C. Felser, Topological materials: Weyl semimetals, Ann. Rev. Condens. Matter Phys. **8**, 337 (2016).

[8] M. Koshino and I. F. Hizbullah, Magnetic susceptibility in three-dimensional nodal semimetals, Phys. Rev. B **93**, 209903 (2015).

[9] S. Borisenko, D. Evtushinsky, Q. Gibson, A. Yaresko, K. Koepernik, T. Kim, M. Ali, J. Brink, M. Hoesch, A. Fedorov, E. Haubold, Y. Kushnirenko, I. Soldatov, R. Schäfer, and R. Cava, Time-reversal symmetry breaking type-II Weyl state in $YbMnBi_2$, Nat. Commun. **10**, 3424 (2019).

[10] Max-Planck Society, The best of two worlds: Magnetism and Weyl semimetals, https://phys.org/news/2019-09-worlds-magnetism-weyl-semimetals.html.

[11] J. R. Soh, P. Manuel, N. Schröter, F. Orlandi, Y. Shi, D. Prabhakaran, and A. Boothroyd, Magnetic and electronic structure of Dirac semimetal candidate $EuMnSb_2$, Phys. Rev. B **100**, 174406 (2019).

[12] Max-Planck Institute for Chemical Physics of Solids, Topological semimetals for potential energy conversion application, https://www.cpfs.mpg.de/2936567/20180914.

[13] K. Byrappa and T. Ohachi (Eds.), *Crystal growth technology* (Springer-Verlag, Berlin, Germany, 2003).

[14] G. Dhanaraj, K. Byrappa, V. Prasad, and M. Dudley (Eds.), *Springer handbook of crystal growth* (Springer-Verlag, Berlin, Germany, 2010).

[15] D. Elwell and H. J. Scheel, *Crystal growth from high-temperature solutions* (Academic Press, London, UK, 1975).

[16] B. R. Pamplin, *Crystal growth* (Pergamon Press, Oxford, UK, 1975).

[17] A. S. Myerson, D. Erdemir, and A. Y. Lee (Eds.), *Handbook of industrial crystallization* (Cambridge University Press, Cambridge, UK, 2019).

[18] X. Y. Liu, - Generic mechanism of heterogeneous nucleation and molecular interfacial effects, in *Advances in crystal growth research*, edited by K. Sato, Y. Furukawa, and K. Nakajima (Elsevier Science B.V., Amsterdam, Netherlands, 2001), pp. 42–61.

[19] Crystallography matters ... more!, https://www.iycr2014.org/participate/crystal-growing-competition-2014/info-for-newcomers/how-to-grow.

[20] M. Tachibana, *Beginner's guide to flux crystal growth* (Springer, Japan, 2017).

[21] J.-Q. Yan, Flux growth utilizing the reaction between flux and crucible, J. Cryst. Growth **416**, 62 (2015).

[22] Introduction to phase diagrams, *Alloy phase diagrams*, vol. 3, *ASM Handbook*, edited by H. Okamoto, M. E. Schlesinger, and E .M. Mueller (ASM International, 2016), pp. 3–16.

[23] A. F. May, M. A. McGuire, and B. C. Sales, Effect of Eu magnetism on the electronic properties of the candidate Dirac material $EuMnBi_2$, Phys. Rev. B **90**, 075109 (2014).

[24] H. Masuda, H. Sakai, M. Tokunaga, Y. Yamasaki, A. Miyake, J. Shiogai, S. Nakamura, S. Awaji, A. Tsukazaki, H. Nakao, Y. Murakami, T. Arima, Y. Tokura, and S. Ishiwata, Quantum Hall effect in a bulk antiferromagnet $EuMnBi_2$ with magnetically confined two-dimensional Dirac fermions, Sci. Adv. **2**, e1501117 (2016).

[25] Y. Shiomi, H. Watanabe, H. Masuda, H. Takahashi, Y. Yanase, and S. Ishiwata, Observation of a magnetopiezoelectric effect in the antiferromagnetic metal $EuMnBi_2$, Phys. Rev. Lett. **122**, 127207 (2019).

[26] Y. Shiomi, H. Masuda, H. Takahashi, and S. lshiwata, Large magneto-piezoelectric effect in $EuMnBi_2$ single crystal at low temperatures, Sci. Rep. **10**, 7574 (2020).

[27] A. Wang, I. Zaliznyak, W. Ren, L. Wu, D. Graf, V. Garlea, J. Warren, E. Bozin, Y. Zhu, and C. Petrovic, Magnetotransport study of Dirac fermions in $YbMnBi_2$ antiferromagnet, Phys. Rev. B **94**, 165161 (2016).

[28] M. Chinotti, A. Pal, W. Ren, C. Petrovic, and L. Degiorgi, Electrodynamic response of type II Weyl semimetal $YbMnBi_2$, Phys. Rev. B **94**, 245101 (2016).

[29] D. Chaudhuri, B. Cheng, A. Yaresko, Q. Gibson, R. Cava, and N. Armitage, An optical investigation of the strong spin-orbital coupled magnetic semimetal $YbMnBi_2$, Phys. Rev. B **96**, 075151 (2017).

[30] J. Liu, J. Hu, D. Graf, T. Zou, M. Zhu, Y. Shi, S. Che, S. Radmanesh, J. Lau, L. Spinu, H. Cao, X. Ke, and Z. Mao, Unusual interlayer quantum transport behavior caused by the zeroth landau level in $YbMnBi_2$, Nat. Commun. **8**, 646 (2017).

[31] J. R. Soh, H. Jacobsen, B. Ouladdiaf, A. Ivanov, A. Piovano, T. Tejsner, Z. Von, H. Wang, H. Su, Y. Guo, Y. Shi, and A. Boothroyd, Magnetic structure and excitations of the topological semimetal $YbMnBi_2$, Phys. Rev. B **100**, 144431 (2019).

[32] A. Sapkota, L. Classen, M. Stone, A. Savici, V. Garlea, A. Wang, J. Tranquada, C. Petrovic, and I. Zaliznyak, Signatures of coupling between spin Waves and Dirac fermions in $YbMnBi_2$, Phys. Rev. B **101**, 041111 (2020).

[33] E. Brechtel, G. Cordier, and H. Schäfer, Zur darstellung und struktur von $CaMnBi_2$ / On the preparation and crystal structure of $CaMnBi_2$, Z. Naturforsch. B **35**, 1 (1980).

[34] S. Klemenz, S. Lei, and L. Schoop, Topological semimetals in square-net materials, Ann. Rev. Mater. Res. **49**, 185 (2019).

[35] M. Farhan, G. Lee, and J. Shim, $AEMnSb_2$ (AE = Sr, Ba): A new class of Dirac materials, J. Phys. Condens. Matter **26**, 042201 (2014).

[36] J. Park, G. Lee, F. Wolff-Fabris, Y. Koh, M. Eom, Y. Kim, M. Farhan, Y. Jo, C. Kim, J. Shim, and J. Kim, Anisotropic Dirac fermions in a Bi square net of $SrMnBi_2$, Phys. Rev. Lett. **107**, 126402 (2011).

[37] S. Blanchard, F. Neese, E. Bothe, E. Bill, T. Weyhermüller, and K. Wieghardt, Square planar vs tetrahedral coordination in diamagnetic complexes of nickel(II) containing two bidentate pi-radical monoanions, Inorg. Chem. **44**, 3636 (2005).

[38] Tetrahedral vs. square planar complexes, https://chem.libretexts.org/bookshelves/inorganic_chemistry/modules_and_websites_(inorganic_chemistry)/crystal_field_theory/tetrahedral_vs._square_planar_complexes.

[39] B. Lv, T. Qian, and H. Ding, Angle-resolved photoemission spectroscopy and its application to topological materials, Nat. Rev. Phys. **1**, 1 (2019).